Molecular Cell

Article

Cell-surface RNA forms ternary complex with RNA-binding proteins and heparan sulfate to recruit immune receptors

Graphical abstract

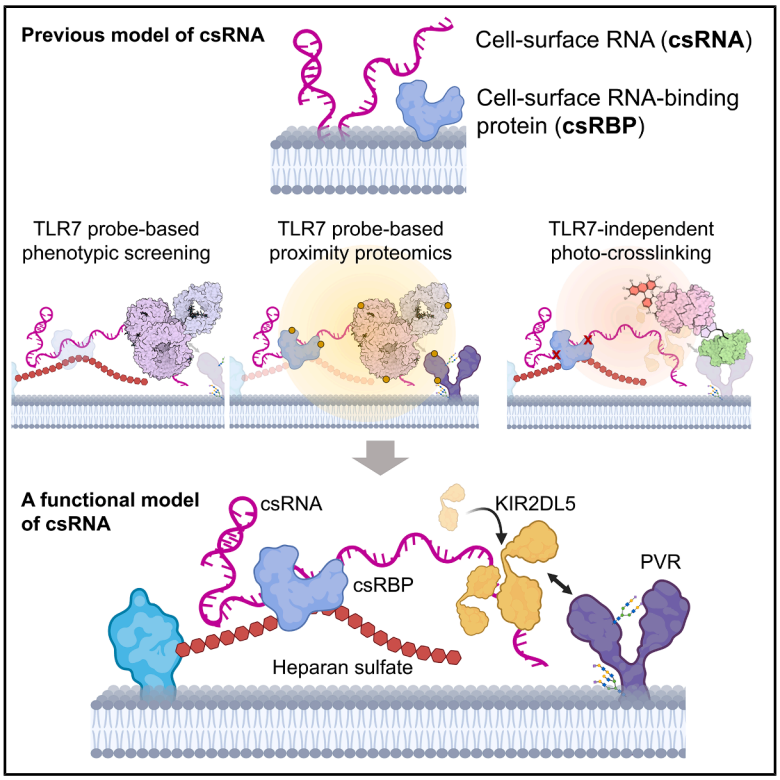

Highlights

- Toll-like receptor 7 (TLR7) was established as a probe for cell-surface RNA (csRNA)
- Heparan sulfate (HS) is essential for RNA cell-surface association
- HS, RNA, and RNA-binding proteins form ternary complexes on the cell surface
- An immune receptor, KIR2DL5, binds to csRNA

Authors

Zeshi Li (李泽实), Bhagyashree S. Joshi, Hongbo Yin (尹泓博), ..., Michiel Vermeulen, Vered Raz, Chirlmin Joo (주철민)

Correspondence

z.li@uu.nl (Z.L.),
v.raz@lumc.nl (V.R.),
c.joo@tudelft.nl (C.J.)

In brief

Li and Joshi et al. describe a molecular model by which RNA is stably presented on the surface of living cells. By forming complexes with RNA-binding proteins and heparan sulfate, cell-surface RNA can recruit immune receptors. Our findings lay the groundwork for investigating how cell-surface RNA contributes to immune modulation.

Li et al., 2025, Molecular Cell *85*, 4633–4650
December 18, 2025 © 2025 Elsevier Inc. All rights are reserved, including those for text and data mining, AI training, and similar technologies.
https://doi.org/10.1016/j.molcel.2025.11.020

CellPress

Molecular Cell

CellPress

Article

Cell-surface RNA forms ternary complex with RNA-binding proteins and heparan sulfate to recruit immune receptors

Zeshi Li (李泽实),[1,2,3,15,16,*] Bhagyashree S. Joshi,[2,13,15] Hongbo Yin (尹泓博),[3] Ruud H. Wijdeven,[4,14] Azen Koç,[3] Dick W. Zijlmans,[5] Irene Santos-Barriopedro,[5] Hailiang Mei,[6] Wei Wu (吴畏),[3] Milad Shademan,[1] Filip M. Zawisza,[3] Eric Bos,[7] Pradeep Chopra,[8] Marvin E. Tanenbaum,[2,9] Thomas H. Sharp,[7,10] Michiel Vermeulen,[5,11] Vered Raz,[1,*] and Chirlmin Joo (주철민)[2,12,*]

[1]Human Genetics Department, Leiden University Medical Centre, 2333 ZC Leiden, the Netherlands
[2]Department of BioNanoScience, Kavli Institute of Nanoscience Delft, Delft University of Technology, 2629 HZ Delft, the Netherlands
[3]Division of Chemical Biology & Drug Discovery, Utrecht Institute for Pharmaceutical Sciences, Utrecht University, 3584 CG Utrecht, the Netherlands
[4]Department of Cell and Chemical Biology, Oncode Institute, Leiden University Medical Center, 2333 ZA Leiden, Zuid-Holland, the Netherlands
[5]Department of Molecular Biology, Faculty of Science, Radboud Institute for Molecular Life Sciences (RIMLS), Oncode Institute, Radboud University Nijmegen, Nijmegen 6525 GA, the Netherlands
[6]Sequencing Analysis Support Core, Department of Biomedical Data Sciences, Leiden University Medical Center, Einthovenweg 20, 2333 ZC Leiden, the Netherlands
[7]Department of Cell and Chemical Biology, Leiden University Medical Center, Leiden 2300 RC, the Netherlands
[8]Complex Carbohydrate Research Center, University of Georgia, Athens, GA 30602, USA
[9]Oncode Institute, Hubrecht Institute-KNAW and University Medical Center Utrecht, Uppsalalaan 8, 3584 CT Utrecht, the Netherlands
[10]School of Biochemistry, University of Bristol, Bristol BS8 1TD, UK
[11]Division of Molecular Genetics, Netherlands Cancer Institute, Amsterdam 1066 CX, the Netherlands
[12]Department of Physics, Ewha Woman's University, Seoul 03760, Republic of Korea
[13]Present address: Whitehead Institute for Biomedical Research, Cambridge, MA 02142, USA
[14]Present address: Department of Functional Genomics, Center for Neurogenomics and Cognitive Research (CNCR), Vrije Universiteit Medical Center, 1007 MB Amsterdam, Noord-Holland, the Netherlands
[15]These authors contributed equally
[16]Lead contact
*Correspondence: z.li@uu.nl (Z.L.), v.raz@lumc.nl (V.R.), c.joo@tudelft.nl (C.J.)
https://doi.org/10.1016/j.molcel.2025.11.020

SUMMARY

Recent discoveries have shown the presence of ribonucleic acid (RNA) on the cell surface, defying the view that RNA only functions intracellularly. However, how RNA is presented on the cell surface and what its biological relevance is are poorly understood. We established Toll-like receptor 7 (TLR7) as a cell-surface RNA (csRNA) probe. Employing it in a genome-wide knockout screening, we identified heparan sulfate (HS) as a crucial factor for csRNA presentation. Cell-surface proximity labeling revealed that HS-associated csRNAs (hepRNAs) are in the vicinity of RNA-binding proteins (RBPs). These observations led us to a model wherein cell-surface HS, RNA, and RBP form ternary complexes, validated by our spatio-selective RNA-protein crosslinking technology in a TLR7-orthogonal manner. We further revealed the identities of hepRNA and found that they can recruit the immune receptor killer cell immunoglobulin-like receptor 2DL5 (KIR2DL5), potentially enhancing receptor-ligand interactions. Employing human cell lines, our findings lay the groundwork for investigating how cell-surface ribonucleoproteins contribute to immune modulation.

INTRODUCTION

Ribonucleic acid (RNA) performs many critical cellular functions in both prokaryote and eukaryote cells. Although the localization of RNA was considered primarily intracellular in mammalian cells, emerging studies have indicated that RNA can be displayed on the cell surface. A previous study found that bacterial genome-encoded RNA can be anchored on their cell surface via binding to a protein.[1] Recent studies have shown the presence of RNA on the extracellular part of mammalian cell plasma membranes.[2–5] These cell-surface RNAs (csRNAs) include fragments of messenger and long non-coding RNAs and glycosylated small

All rights are reserved, including those for text and data mining, AI training, and similar technologies.

RNAs. There are indications that csRNAs can participate in molecular recognition, thereby modulating cell-cell interactions. A recent study has shown csRNA-mediated neutrophil recruitment by interacting with P-selectin on the endothelial cells.[6] Despite the aforementioned studies, mechanistic understanding as to how RNAs are stably presented on the mammalian cell surface remains limited. It is also unclear if csRNA may exhibit other modes of function besides presenting glycan moieties to interacting cells.[2,6]

As most RNA molecules are associated with RNA-binding proteins (RBPs), it can be speculated that csRNA is similarly associated with RBPs, providing a mechanism for cell-surface anchoring. In line with this hypothesis, both earlier and recent studies have demonstrated RBPs, previously thought to be localized only intracellularly, are also present on the plasma membrane.[7–10] Thus, the potential binding partners are indeed available for and in proximity to RNA on the cell surface. However, these RBPs are generally soluble proteins that do not possess a transmembrane domain and are therefore unlikely to be directly anchored on the lipid bilayer like many cell-surface glycoproteins. For example, a classical nuclear RBP, U5 SNRNP200, has been evaluated as an acute myeloid lymphoma-associated cell-surface antigen for immunotherapy.[9,10] This RBP was shown to be associated with the Fcγ receptor IIIA. A more recent study revealed that a plethora of RBPs can localize to the cell surface as possible carriers of csRNA.[11] However, it is largely unknown how csRNA and RBPs become stably presented on the plasma membrane, and if so, whether they are associated with each other.

Animal cells employ highly negatively charged linear carbohydrate polymers, such as glycosaminoglycans, as a scaffold to enrich soluble proteins and organize membrane-bound proteins on the plasma membrane.[12] Heparan sulfate (HS) is an important class of glycosaminoglycans ubiquitously found on plasma membranes and in the extracellular matrix.[13] Portions of HS are heavily sulfated and serve as docking sites for a broad array of proteins, including growth factors, morphogens, amyloid proteins, lipoproteins, cytokines, and chemokines, as well as many microbial proteins. HS is characterized by having an extension of repeating disaccharide units, glucosamine-α1,4-glucuronic acid (GlcN-GlcA) or glucosamine-α1,4-iduronic acid (GlcN-IdoA). An HS chain can contain over a hundred monosaccharide units. Glycan modifications such as *N*- and *O*-sulfation introduce negative charges to portions of the HS chain and are known to be crucial for the biological functions of HS. The pattern of *N*- and *O*-sulfation, also known as the sulfation code, critically determines what proteins interact with HS. These features make HS among a main director of cell-surface interactions.[14]

Herein, we demonstrate that HS functions as a scaffold for presenting RNAs and RBPs on the cell surface. A key tool in our study was Toll-like receptor 7 (TLR7), which we leveraged as a probe for csRNA. We established that the recombinant TLR7-Fc fusion protein can effectively detect and capture RNA on living cells, enabling a genome-wide knockout (KO) screening to identify genes regulating csRNA localization. The screening revealed HS biosynthetic enzymes as essential factors. Using the same probe, we also identified the csRNA-proximal proteome, which includes both classical and non-canonical RBPs. These findings led us to propose a model in which RNA, RBP, and HS form ternary complexes for csRNA presentation. To further validate this ternary configuration, we developed a TLR7-independent approach—spatio-selective crosslinking followed by orthogonal organic phase separation (SCOOPS). SCOOPS employs local photocatalytic generation of singlet oxygen (SO) to crosslink RNA with bound proteins, facilitating selective isolation of csRNA. By combining SCOOPS with next-generation sequencing, we identified HS-associated csRNAs and uncovered primary structural imprints contributing to their localization. Finally, we demonstrated that HS-associated csRNAs can recruit killer cell immunoglobulin-like receptor 2DL5 (KIR2DL5) to the cell surface, suggesting a potential role for csRNA in modulating immune interactions between KIR2DL5 on immune cells and its cognate ligand on target cells.

RESULTS

Establishment of TLR7 as a probe for csRNA

The sequence of RNA molecules on the plasma membrane likely varies between different cells, and RNA molecules present at low copy numbers may elude detection.[15] The state-of-the-art csRNA labeling approaches are not compatible with live cells due to fixation or rupturing of the plasma membrane.[3,15] To overcome this, we reasoned that the use of an RNA-recognizing probe with low sequence specificity, rather than a hybridizing probe, which requires prior knowledge of csRNA sequence, should boost the chance for csRNA detection and yield strong signals. We, therefore, exploited nature's RNA-sensing machinery: TLR7,[16] an endosome-localized, pattern recognition receptor in select immune cells to sense both foreign and endogenous single-stranded RNA molecules.[17–19] TLR7 requires two consecutive uridine moieties for strong RNA binding but requires only a few other sequence features.[20] We used the commercially available human Fc-tagged TLR7 ectodomain (Ala27-Asn839), denoted hereafter as TLR7-Fc. TLR7-Fc is expected to recognize csRNA on intact (live) cells and allow for the detection by a secondary antibody for different downstream applications.

We employed confocal microscopy to examine the efficiency of TLR7-Fc to detect csRNA. TLR7-Fc is applied onto intact, fixed cells without cell permeabilization, followed by washing and the addition of a fluorophore-conjugated, anti-human immunoglobulin G (IgG) secondary antibody. To check for localization of TLR7-Fc staining, we labeled the cell surface with biotin-conjugated wheat germ agglutinin (WGA biotin),[21] a lectin that recognizes N-acetylneuraminic acid and N-acetylglucosamine residues present in cell surface glycans, and the biotin moieties were detected by fluorescent streptavidin. We observed that bright puncta given rise to by the TLR7-Fc probe in complex with the fluorescent secondary antibody align with the rims of HeLa, U2OS, and Mel526 cells (Figures 1A, S1A, and S1B). This is akin to many cell surface proteins, which manifest in clusters.[22,23] WGA signal is confined to the cell surface. csRNA signal was absent in controls devoid of TLR7-Fc but only including the secondary antibody (Figure S1C). A treatment with an RNaseA/T1 cocktail in fixed, non-permeabilized cells severely disrupted the TLR7 signal (Figure 1A), while DNase treatment did not (Figure S1D), validating the RNA specificity

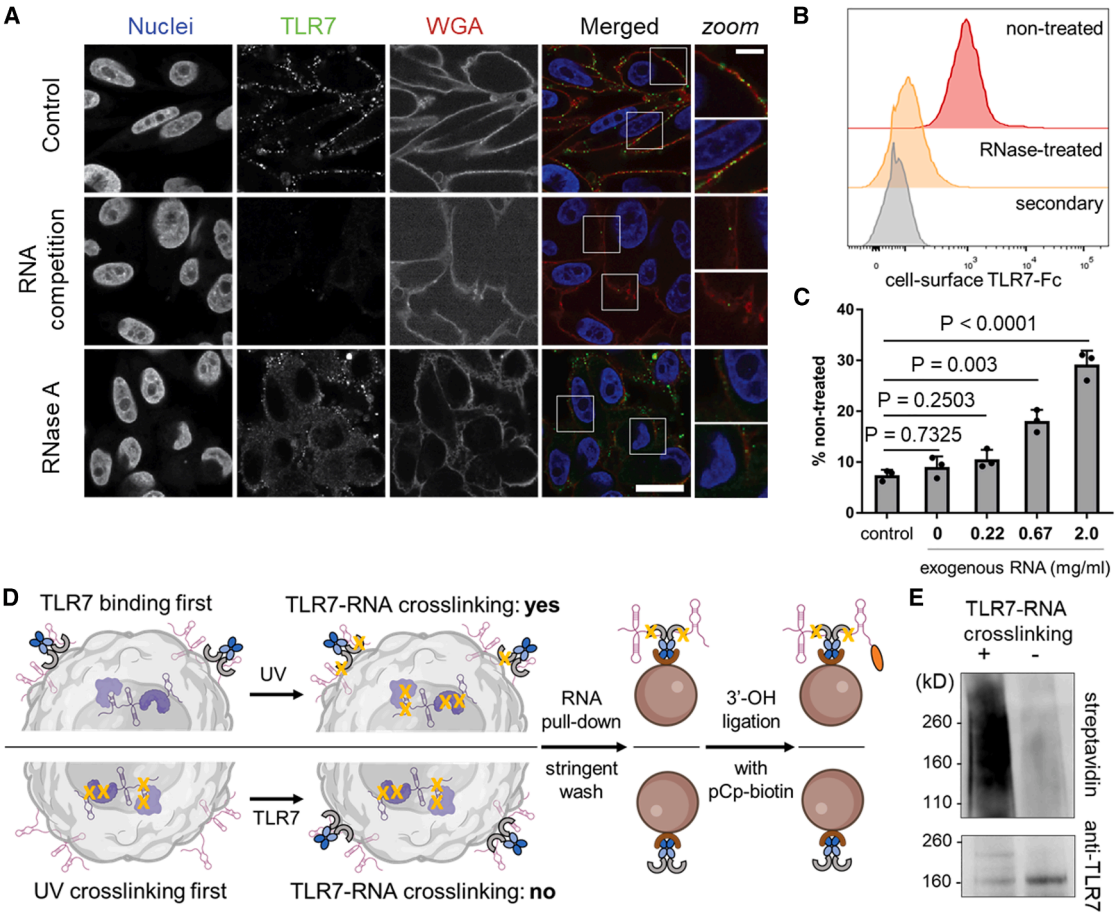

Figure 1. TLR7-Fc is a csRNA probe

(A) Confocal microscopy images of csRNA on Mel526 cells probed by TLR7-Fc and Alexa Fluor 488-conjugated goat-anti-human IgG. Cell surface was stained by WGA biotin and streptavidin-Alexa Fluor 594. See supplemental information for the sequence of competitor single-stranded RNA (ssRNA). RNase A concentration, 40 μg/mL. Nuclear counterstaining: DAPI. Scale bar: 20 μm. Images are representative of 3 independent experiments.

(B) Histograms from flow cytometry analysis of csRNA on Mel526 cells probed by TLR-Fc in complex with goat-anti-human-Alexa Fluor 647. 40 μg/mL RNase A was used to deplete csRNA during EDTA lifting. $n = 3$ independent cell cultures.

(C) TLR7-Fc binding was rescued by exogenous total RNA in a concentration-dependent manner. Exogenous RNA in 1× DPBS was added to cells at 4°C. 0 mg/mL RNA means 1× DPBS buffer without RNA. The control was with cells treated with RNase A but without any additional incubation. *y* axis shows relative signal intensity, with the geometric mean of TLR7 binding on non-RNase-treated cells set to 100%. $n = 3$ independent cell cultures. Error bars represent SD.

(D) Schematics of *in situ* crosslinking and csRNA capture experiment. pCp, cytidine-5′-phosphate-3′-(6-aminohexyl)phosphate. Orange oval represents biotin.

(E) Chemiluminescent detection of TLR7-captured and biotin-labeled RNA. Rabbit anti-TLR7 was used to check for TLR7-Fc on the same nitrocellulose membrane after blotting biotinylated RNA. $n = 3$ independent cell cultures for crosslinked and non-crosslinked samples.

of TLR7 binding. Moreover, the pre-saturation of TLR7-Fc with an exogenous, synthetic single-stranded RNA competitively inhibited TLR7 binding, further supporting the specificity of TLR7 to probe RNA on cells.

Live-cell staining with TLR7 showed the same puncta pattern, indicating that the clustering of our probe on the cell surface is unlikely to be caused by cell fixation (Figure S1E).[24–26] Interestingly, the monoclonal antibody J2, previously used for intracellular detection of endogenous double-stranded RNA (dsRNA)[27] and viral dsRNA,[28] as well as for cell-surface glycoRNA,[2] did not give detectable signals on HeLa or U2OS cell surface (Figure S1F). Next, to observe csRNA in a more detailed subcellular context, we employed electron microscopy (EM), leveraging the TLR7-Fc probe and protein-A-gold (10 nm) as a secondary probe (Figures S1G and S1H). We observed csRNA signals along the cellular periphery, cell-cell junctions, and endocytosed vesicles, confirming the findings with fluorescent microscopy.

We further used our TLR7-Fc probe to quantify csRNA and its sensitivity to RNase treatment with flow cytometry (Figure 1B; see Figure S1I for gating). Corroborating the fluorescence imaging results, when live cells were pre-treated with RNase A, the signal intensity given rise by TLR7-Fc in complex with the fluorescent secondary antibody dropped dramatically close to the background. To further confirm that TLR7-Fc binds to RNA on the cell surface, the prior csRNA-depleted cells by RNase were incubated with exogenous, purified total cellular RNA (Figure S1J). We found that TLR7 binding could be partly restored by exogenous RNA in a concentration-dependent manner (Figure 1C).

To further validate that TLR7 binds to RNA on the cell surface, we performed *in situ* RNA-protein crosslinking with ultraviolet-C (UVC) after TLR7-Fc probe addition, followed by RNA precipitation and RNA 3′ end labeling (Figure 1D). Upon UVC irradiation, csRNA is expected to be covalently bound to the TLR7-Fc probe and can be co-precipitated with the probe using protein A-functionalized magnetic beads. The precipitated RNA was then labeled at the 3′ end with biotin-cytidine using RNA ligase 1. This was followed by SDS-PAGE and western blot for biotin. As a negative control, cells were UVC irradiated before TLR7-Fc incubation and subjected to the same procedure. UVC-crosslinked biotinylated csRNA is expected to remain bound to TLR7 throughout the entire procedure, whereas the csRNA not crosslinked to TLR7 will dissociate upon denaturation and therefore will not remain on the membrane.[29] We observed a strong chemiluminescent signal above TLR7-Fc molecular weight for crosslinked csRNA-TLR7 (Figure 1E) but not for non-crosslinked TLR7 probe. The results demonstrate TLR7 probe indeed binds to RNA on the cell surface.

To confirm TLR7-Fc binding to RNA is mediated by the TLR7 ectodomain but not other portions of the protein (such as the Fc tag), we performed an *in vitro* RNA crosslinking and co-precipitation assay using the TLR7-Fc and human IgG control. Fragmented, purified total cellular RNA was incubated and crosslinked (irradiated with UVC, 254 nm) with TLR7-Fc and IgG, pulled down on beads and intensively washed, labeled with Cy5 at the 3′ end, and finally released from beads by Proteinase K digestion. Purified precipitated RNA was then analyzed in agarose gel electrophoresis. Strong fluorescent bands were observed for TLR7-Fc captured RNA but not for IgG control (Figure S1K). The results indicated the Fc tag did not non-specifically bind to RNA, demonstrating the RNA specificity of our probe.

Genome-wide screening identified essential factors for RNA presentation at the cell surface

To uncover the molecular underpinnings of csRNA presentation. We performed a pooled genome-wide, CRISPR-Cas9-mediated KO screening[30] to identify essential cellular factors for csRNA stable presentation. TLR7-Fc in complex with a fluorescent secondary antibody was used to enrich the csRNA^{low} population with fluorescence-assisted cell sorting (FACS). Such FACS-based enrichment was performed twice. The enriched cells, together with the non-enriched input cells, were subjected to deep sequencing to identify the guide RNAs (gRNAs) of CRISPR-Cas9 giving rise to the csRNA^{low} phenotype. (Figure 2A; see Figure S2A for gating). Likewise, the csRNA^{high} phenotype was also enriched and sequenced.

Data analysis revealed that enzymes involved in HS biosynthesis[31] were among the most highly scored hits, suggesting HS is a pivotal molecular factor for the stable cell-surface display of RNAs (Figure 2B; full list of hits in Table S1). Our hits include enzymes for the core tetrasaccharide synthesis (XYLT2, B4GALT7, B3GALT6, and B3GAT3), glycan chain polymerizing enzymes (EXT1, EXT2, and EXTL3), as well as glycan chain modifying enzymes such as sulfotransferases (NDST1, HS2ST1, and HS6ST1) and a xylose kinase (FAM20B) (Figure 2C). These hits suggest the stable presentation of csRNA requires a fully extended HS chain and an appropriate *N*- and *O*-sulfation pattern.

Apart from the HS-related glycosyltransferases and glycan-modifying enzymes, we also identified regulators in HS biosynthesis. For example, uridine diphosophate (UDP)-glucose 6-dehydrogenase (UGDH) oxidizes UDP-linked glucose (UDP-Glc) to UDP-GlcA, a glycosyl donor for HS polymerization; SLC35B2 is a Golgi membrane transporter of the sulfo-donor, adenosine 3′-phospho-5′-phosphosulfate[32]; SLC10A7 is crucial for cellular calcium regulation and was implicated in HS biosynthesis[33]; and C3orf58 has been recently shown to regulate HS biosynthesis.[34] The genes related to the *N*-glycan biosynthetic pathway were not among the candidates, suggesting the csRNA detected by TLR7 is independent from glycoRNA, and it does not require *N*-glycosylation to access the plasma membrane. Interestingly, the genetic screening also revealed several classical or non-canonical RBPs as essential factors for csRNA (see Table S1 for their reported functions), including an ATP-dependent RNA helicase DEAH box protein 29 (DHX29), transmembrane emp24 domain-containing protein 10 (TMED10), UGDH, and transmembrane 9 superfamily member 3 (TM9SF3).

From the csRNA^{high} phenotype (see Table S2 for the full list), the significantly enriched hits consistent in two biological replicates included only N-acylneuraminate cytidylyltransferase (CMAS), uroporphyrinogen decarboxylase (UROD), and C-type lectin domain family 17, member A (CLEC17A).

Validation of genome-wide screening

Next, attention was focused on validating HS as a necessary biomolecule for RNA's display on the cell surface. csRNA location closely correlated with the HS staining on the cell surface, showing their tight proximity (Figure 2D). We then generated HS-deficient mutant cells lacking either the elongation enzyme EXT2 or sulfotransferase HS6ST1 via CRISPR-Cas9-mediated KO, each with two high-scoring gRNAs from the screen, and used flow cytometry to quantify TLR7-Fc binding. Both gRNAs for EXT2 resulted in an almost complete loss of TLR7-Fc binding. One gRNA for HS6ST1 led to a similar phenotype as did EXT2 KO, whereas the other gRNA reduced TLR7-Fc binding down to approximately 30% of the wild type (Figure 2E). Confocal microscopy also showed a dramatic reduction in csRNA signal around the cell rim after knocking out EXT2, HS6ST1, EXTL3, and C3orf58 (Figure S2B). In addition to using Mel526 cells, reduced TLR7-Fc binding to the cell rim was also observed in Chinese hamster ovary (CHO) cell mutants (pgsD-677 and pgsE-606), which are deficient in HS biosynthesis, compared with wild-type CHO cells (Figure S2C).

An alternative scenario that might have given rise to similar hits in our genome-wide screening would be that TLR7-Fc directly binds to HS on the cell surface (Figure S2D). Thus, the loss of TLR7 binding to the cell surface would have been caused by the RNase non-enzymatically and competitively suppressing TLR7-Fc binding to HS. To exclude this, we compared the TLR7-Fc to well-studied HS-binding proteins using flow cytometry, including fibroblast growth factor-2 (FGF2) and an anti-HS IgM 10E4.[35] All proteins bound to the wild-type cell surface strongly but hardly to EXT2-KO cells, confirming the HS dependency of the tested proteins (Figure S2E). However, the two HS binders differed

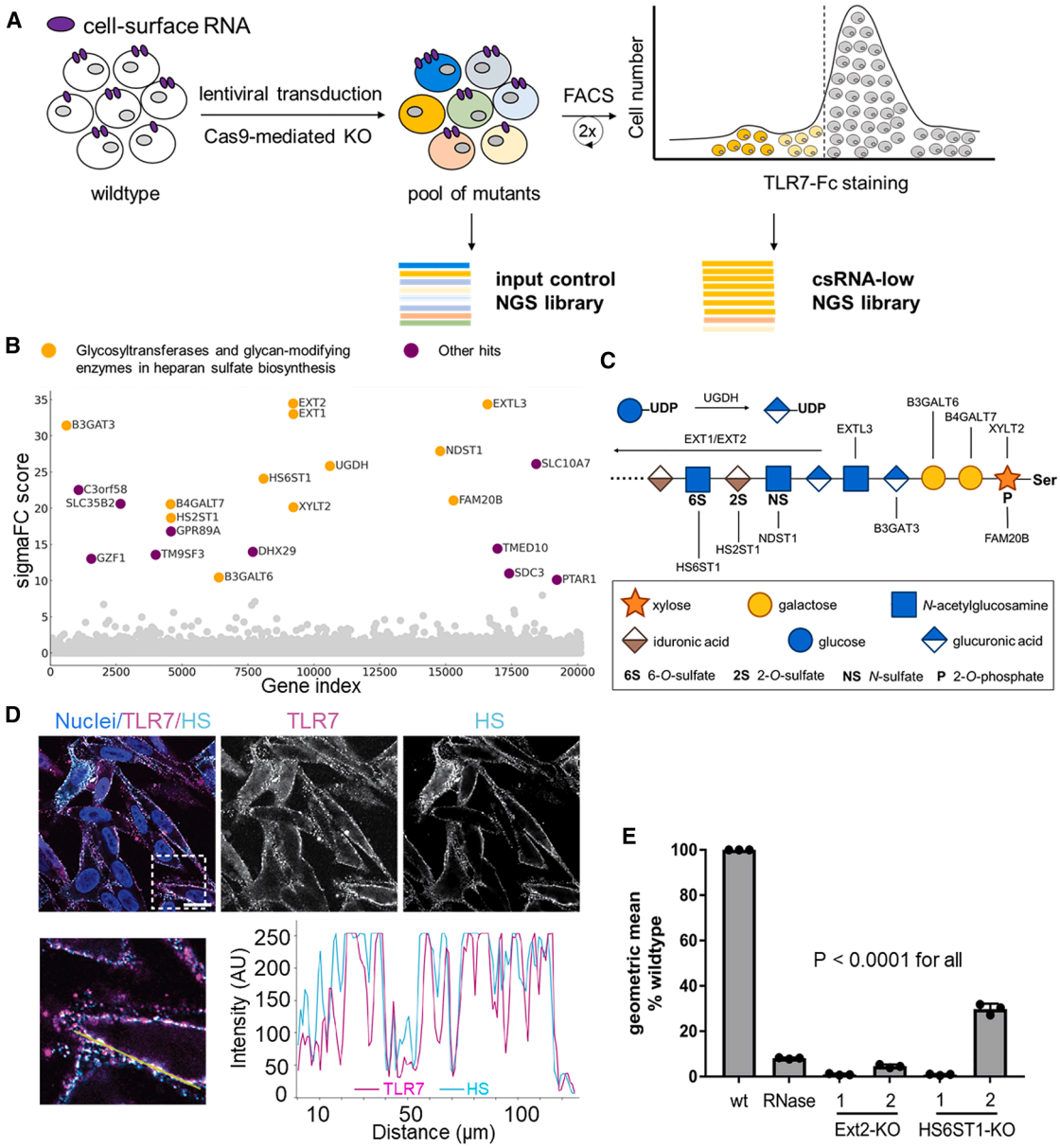

Figure 2. Genome-wide screening reveals essential factors for csRNA stable presentation

(A) Schematics of the genetic screen in Mel526 cells with csRNA stained with TLR7-Fc and Alexa Fluor 488-conjugated goat-anti-human IgG. Color-coded cells represent the 5% of cells with the lowest fluorescent signal, indicating the loss of csRNA.

(B) Dot plot of genetic screening results. *y* axis in this plot is the geometric mean of the sigmaFC scores from the duplicates calculated using PinAPL-Py. HS-related glycosyltransferases and glycan-modifying enzymes are colored in yellow. Other hits with a sigmaFC larger than 10 are colored in purple.

(C) HS biosynthetic pathway. Gene candidates as yellow dots in (B) are shown in this schematic representation.

(D) csRNA and HS colocalization on the cell surface of Mel526. csRNA was probed by TLR7-Fc and Alexa Fluor 647-conjugated rat anti-human IgG (magenta), while HS was labeled with mouse anti-HS (10E4 epitope) antibody and Alexa Fluor 488-conjugated goat anti-mouse IgM mu chain secondary antibody (cyan). The line intensity profile along the yellow line shows csRNA tightly overlaps with HS. Nuclear staining (blue): DAPI. Scale bar: 20 μm. The frame with the dashed line indicates the area where the intensity profile was collected. Images are representative of 3 independent experiments.

(E) Flow cytometry analysis showing csRNA loss in EXT2 and HS6ST1 KO mutant Mel526 cells. TLR7-Fc with goat-anti-human-Alexa Fluor 647 was used for csRNA staining. 40 μg/mL RNase A-treated cells are used as control. The numbers above EXT2 and HS6ST1 represent different gRNAs for KO (see STAR Methods for sequences). $n = 3$ independent cell cultures. Error bars represent SD.

from TLR7 by that they were refractory toward RNase treatment. In addition, we performed surface plasmon resonance binding studies of the RNase (Purelink RNase A) used in the above studies with heparin-coated chips (Figure S2F). No signal was detected across all RNase concentrations, suggesting the RNase used in the study did not bind to HS and was therefore unlikely to

competitively suppress other proteins for HS binding. These results demonstrated its loss of TLR7-Fc binding to the cell surface was due to the RNase-mediated digestion of csRNA.

To further validate the genetic screen results, we selected two HS-deficient mutant cells for the TLR7 binding rescue experiment by exogenous total RNA. Cells were first treated with RNase A and then with total RNA fragments at varying concentrations (Figure S2G). The treated cells were then incubated with TLR7-Fc, followed by a fluorescent secondary antibody. The TLR7 binding remained close to the background throughout all experimental groups regardless of the RNA concentrations. These results demonstrated that cells lacking an extended HS chain or an appropriate sulfation pattern become refractory to exogenous RNA incubation and can no longer rescue TLR7 binding, suggesting that csRNA presentation requires intact HS. Hereafter, we refer to the csRNA detected by the TLR7-Fc probe as HS-associated csRNA (hepRNA).

RNA, RBP, and HS are in the vicinity on cell surface

Both RNA and HS are highly negatively charged biopolymers. How are these two macromolecules associated? We were struck by the observation that upon proteolytic detachment of adherent cells by a recombinant protease TrypLE Express before flow cytometry, TLR7-Fc was no longer detectably bound to the cell surface (Figure S3A), while non-tryptic detachment methods such as EDTA allowed for hepRNA detection by TLR7-Fc (Figure 1B). The observation led us to hypothesize that hepRNA may require an additional factor, such as proteins, to be presented on the cell surface HS (Figure S3B). We, therefore, applied a peroxidase-mediated proximity labeling approach[36] to identify the hepRNA-proximal proteome using TLR7-Fc. Peroxidase-mediated proximity labeling has been shown to exhibit particularly high efficiency within the radius of ~20 nm due to the direct contact of the peroxidase catalytic center with proximal proteins. Decreased, but considerable labeling does occur within a radius of ~270 nm,[37,38] due to the diffusion of peroxidase-activated biotin-phenol radical.[38] Thus, peroxidase-based proximity labeling is expected to afford protein candidates that are direct binders of hepRNA and those that do not physically interact with hepRNA but are spatially close to it.

We pre-complexed TLR7-Fc with horseradish peroxidase (HRP)-conjugated protein A, which was then incubated with untreated and RNase A-pre-treated Mel526 cells (Figure 3A). RNase treatment is expected to digest unprotected regions of all csRNA, whereas the portions proximal to or bound by a protein are protected from digestion (Figure 3B), an effect commonly exploited to study proteins' footprint on an RNA.[29,39] As an isotype control, human IgG was used instead of TLR7-Fc. Biotinylation of proteins on the cell surface was confirmed by fluorescence imaging and western blot (Figures S3C and S3D). Following proximity labeling, biotinylated proteins were enriched from cell lysate with streptavidin-functionalized beads. Bound proteins were then subjected to LC-MS/MS and label-free quantitative proteomics analysis.

By comparing the TLR7-proximal proteome of cells without RNase treatment (denoted as "TLR7") to that of the IgG isotype control, we identified 315 proteins as significantly enriched hits (fold-change [FC] ≥ 4 and p value < 0.01). Full list of identified proteins in Table S3). Of the significantly enriched hits, 137 of them carry the Gene Ontology (GO) term "cell surface" (GO:0009986) or "extracellular region" (GO:0005576), including known glycoproteins and glycosylphosphatidylinositol-anchored proteins (Figure 3C). 76 of the cell-surface (glyco)proteins were not anymore enriched over IgG control in the RNase-treated cell dataset (denoted as "RNase") (Figure S3E), which suggested upon extracellular RNase digestion, hepRNA is no longer proximal to the (glyco)proteins.

Across the TLR7 and RNase datasets, a considerable number of proteins remained consistently enriched, with a similar FC (vs. IgG control) in both datasets (Figures 3D and S3F; see the full list in Table S4). These proteins likely had been proximity-biotinylated by the residual TLR7-Fc:protein A-HRP complex bound to the RNase-truncated hepRNA (Figure S3G). We queried RBP2GO, a database documenting validated and putative RBPs, with the overlapping hits from TLR7 and RNase samples. It returned with a match of 137 proteins. The 137 RBP2GO-documented hits include classical RBPs such as heterogeneous nuclear ribonucleoprotein A1 and A2B1 (HNRNPA1 and HNRNPA2B1, respectively), and Sjögren syndrome antigen B (SSB), all of which bear a high RBP2GO score, indicating high confidence for direct RNA binding. Non-canonical RBPs that do not possess a classical RNA-binding domain were also among the hits, many of which are metabolic enzymes or chaperones with moonlighting RNA-binding functions, such as enolase 1 (ENO1)[40] and calreticulin (CALR).[41] These proteins are normally scored moderately in the RBP2GO database.

We next asked if the detection of the RBPs was due to cell-surface localization or as a result of labeling/enrichment of intracellular components. We selected both classical and non-canonical RBP hits spanning a wide range of RBP2GO scores for immunofluorescence imaging to determine their localization (Figures 3E–3H). All the tested proteins, including HNRNPA1, SSB, proliferation-associated gene 2G4 (PA2G4), and ENO1, were found on the cell surface, and they were partially colocalizing with TLR7-Fc, suggesting hepRNA and a fraction of these RBPs are in the vicinity. Flow cytometry analysis of cell-surface HNRNPA1 and ENO1 (Figure S3H) in the EXT2-KO cells showed that the HS deficiency resulted in a loss of the cell-surface localized RBPs (csRBPs). Western blot of whole-cell lysate from wild-type and EXT-KO cells confirmed the absence of csRBP was due to the lack of HS as a scaffold on the cell surface but not a global reduction of protein expression because of HS deficiency (Figure S3I).

hepRNA, csRBP, and HS form ternary complexes

Next, we sought to further elucidate the hepRNA molecular configuration. We have shown the cell surface presentation of hepRNA and csRBP is dependent on intact HS, suggesting a scaffolding role of HS. The spatial proximity of csRBP, hepRNA, and HS prompted us to hypothesize that the three biomolecules form ternary complexes on the cell surface. To validate this model, we introduce herein a facile strategy for cell-surface RNP *in situ* crosslinking and isolation, termed SCOOPS. Key to SCOOPS was an unexpected finding that SO, a highly reactive oxygen species, can lead to RNA-protein crosslinking (Figure S4), an effect analogous to conventional UV irradiation. However, unlike UV crosslinking, which can only be applied to whole cells, numerous reports found that SO can be generated

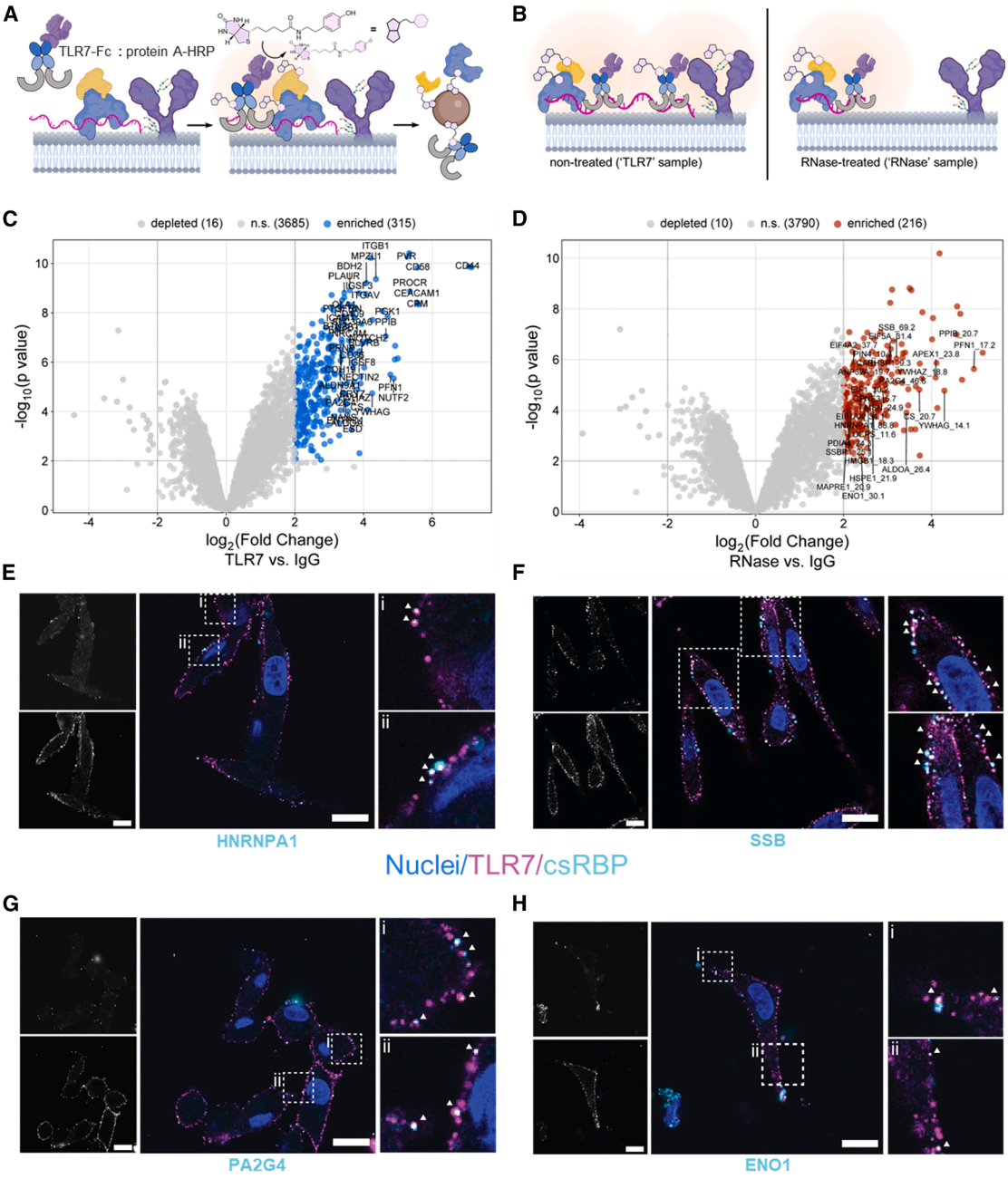

Figure 3. TLR7-proximal proteome harbors known RBPs

(A) Schematics of TLR7-mediated proximity labeling to identify hepRNA-proximal proteome. As negative control, IgG was used instead of TLR7-Fc for forming complex with protein A-HRP.

(B) Extracellular RNase-treated cells were also proximity-labeled in the same fashion.

(C) Volcano plot from the comparison of proteomes between TLR7-mediated proximity labeling and IgG control. hepRNA-proximal candidates (FC $\geq$ 4, $p < 0.01$) are shown in blue. Classically cell-surface localized proteins are labeled with their names. $n = 3$ independent cell cultures.

(D) Volcano plot from the comparison of proteome between TLR7-mediated proximity labeling post-RNase treatment and IgG control. hepRNA-proximal candidates are shown in red. RBP2GO database-documented proteins (RBP2GO score > 10) are labeled with their names and the RBP2GO scores.

(E–H) Confocal microscopy was performed to confirm cell-surface colocalization with hepRNA for select csRBP candidates. The csRBPs were detected with rabbit anti-RBP antibodies and Cy3-conjugated goat anti-rabbit secondary antibody. Nuclear staining: DAPI. Scale bars: 20 μm. Images are representative of 2 independent experiments.

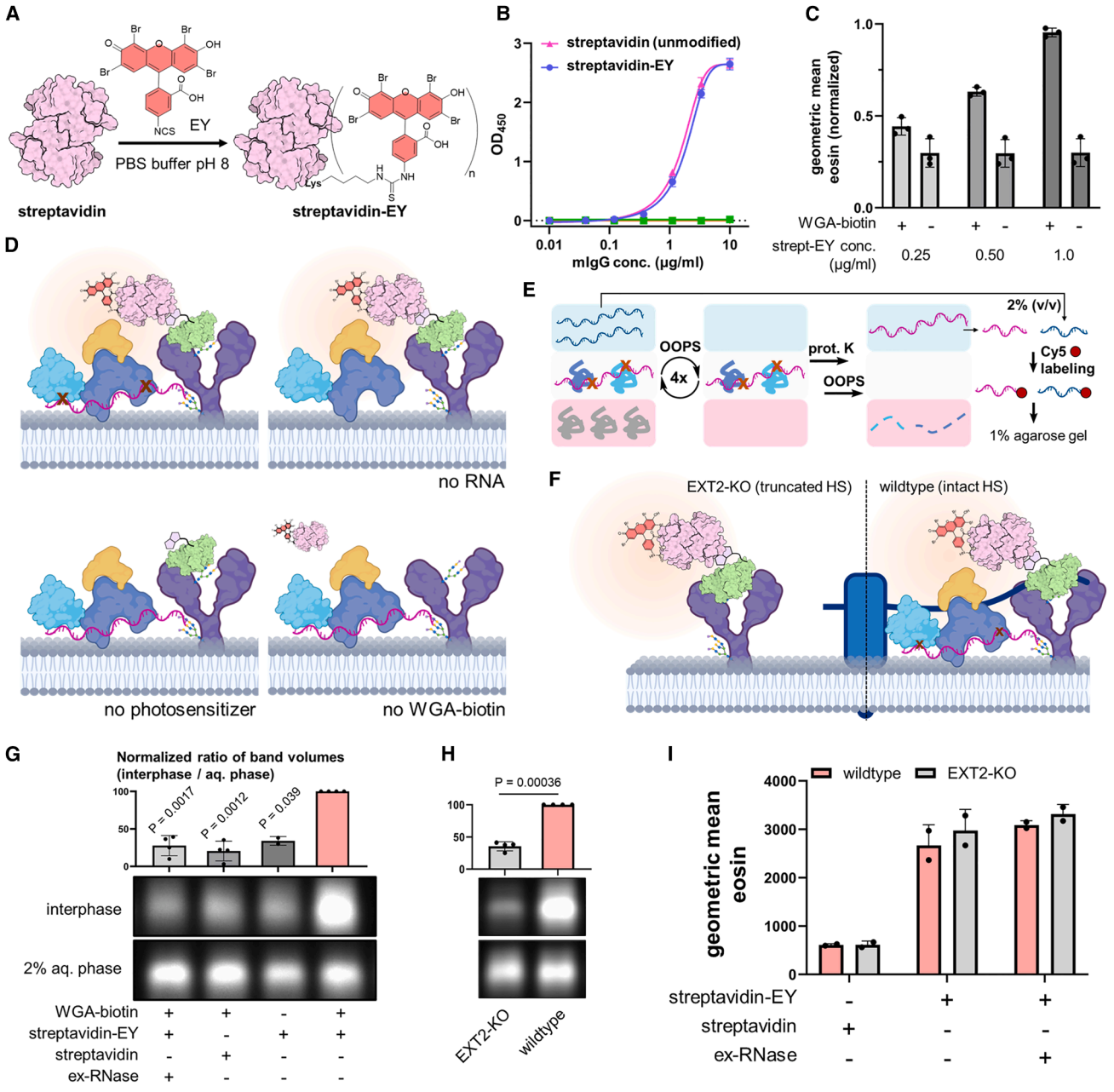

Figure 4. hepRNA HS-dependency validation by TLR7-independent cell-surface crosslinking experiments

(A) Reaction scheme for eosin isothiocyanate (EY)-streptavidin conjugation. Isothiocyanate generally react with primary amines on proteins, forming thiourea.

(B) Enzyme-linked immunosorbent assay (ELISA) demonstrates modified streptavidin retains full capacity for biotin binding. Blue circle, with streptavidin-EY coated on the plate, incubated biotinylated IgG; pink triangle, unmodified streptavidin, biotinylated IgG; green square, streptavidin-EY, unmodified IgG; orange triangle (inverted), unmodified streptavidin, unmodified IgG. *n* = 3 experiments performed on different days. Error bars represent SD.

(C) Titration of streptavidin-EY on live-cell surface with and without biotinylated WGA deposition. *n* = 3 independent cell cultures. Error bars represent SD.

(D) Schematics of EY-mediated cell-surface crosslinking experiment and controls. In the no-RNA control, live cells were pre-treated with RNase I.

(E) Sample processing after live-cell-surface crosslinking. Abbreviations are as follows: OOPS, orthogonal organic phase separation; prot.K, Proteinase K; Cy5, for this experiment, cyanine 5-conjugated cytidine-5′-phosphate-3′-(6-aminohexyl)phosphate.

(F) Schematics of EY-mediated cell-surface crosslinking on wild-type and HS-deficient cells.

(G) 1% agarose gel electrophoresis of 3′ end Cy5-labeled RNA from samples depicted in (D). Gel images were cropped for the small RNA region. Bar graphs show the normalized band volumes corrected by aqueous phase total RNA. *n* = 4 independent cell cultures; *n* = 2 for no-WGA-biotin control. Error bars represent SD.

(legend continued on next page)

locally within a subcellular region due to its transient nature (half-life in water ~4 μs[42]) to achieve spatio-selective chemistry.[43–45] Therefore, we envisioned that by tethering a SO generator to cell surface, locally produced SO could lead to crosslinking of RNA to bound proteins selectively at cell surface.

After cell-surface crosslinking, RNA-protein complexes on the cell surface become covalently bound and will exhibit an amphiphilic nature, which is leveraged in OOPS for their isolation. In OOPS, cells are lysed in acid guanidinium thiocyanate-phenol-chloroform (AGPC). While free RNA and proteins are partitioned into the aqueous and the organic phases, respectively, the amphiphilic crosslinked RNPs are in between the two phases and form a thickened interphase.[46–48] Repetitive cycles of phase separation effectively wash away interphase-trapped non-crosslinked RNA and proteins.

To establish SCOOPS for cell-surface biomolecules, we tethered a small-molecule SO generator, eosin Y (EY), onto streptavidin (strep-EY). Strep-EY retained full binding capacity to biotin (Figures 4A and 4B) and can be recruited to the cell surface by WGA biotin (Figure 4C). We expect the AGPC interphase to contain crosslinked csRNA-protein only when csRNA is intact and when both WGA biotin and strep-EY are present, while missing out on any component would afford little, if any, csRNA after SCOOPS (Figure 4D). To perform SCOOPS, cells were incubated sequentially with WGA biotin and strep-EY and were subjected to AGPC immediately after green light irradiation.

The crosslinked csRNA (pink RNA in Figure 4E) was then released by proteinase digestion of the AGPC interphase after repetitive washes. The released csRNA was then fluorescently ligated at the 3′ end and subjected to agarose gel electrophoresis. A small portion of total RNA (blue RNA in the first aqueous phase in Figure 4E) was also taken along and processed in the same fashion to ensure the inputs for AGPC are consistent across different samples. A strong fluorescent signal of released interphase RNA was observed only when both strep-EY and WGA biotin are present (the fourth lane of Figure 4G). Leaving out either component afforded much weaker signals (the second and third lanes). Pretreating live cells briefly with extracellular RNase to degrade csRNA (first lane) resulted in a significantly weakened signal compared with untreated, csRNA-intact cells.

We then employed SCOOPS to validate HS's essential role in presenting hepRNA-RBP complexes at the cell surface. We expected cells deficient in HS biosynthesis should afford less SCOOPS-isolated RNA due to the absence of the intact polysaccharide chain as a scaffold for hepRNA presentation (Figure 4F). We observed a significant reduction of SCOOPS-isolated RNA fluorescence from HS-deficient cells compared with the wild-type cells (Figure 4H). To ensure the reduced signal was caused by the biology rather than differences in SO generator recruitment on the cell surface, we performed flow cytometry assays to quantify recruited strep-EY on wild-type and HS-deficient cells (Figure 4I). We found strep-EY introduction to the cell surface was at a comparable level between wild-type and the HS-deficient cells. Taken together, the results demonstrated that a portion of SCOOPS-isolated RNA becomes largely absent in the HS-deficient cells. These results validated the observation made with the TLR7 probe in an orthogonal manner and suggest that hepRNA is dependent on the intactness of HS for a stable presentation on the cell surface.

hepRNA identification by sequencing of SCOOPS-isolated RNAs

We have demonstrated biochemically that hepRNA could be enriched via SCOOPS, and we sought to identify the SCOOPS-isolated RNA species. Bioanalyzer traces revealed that SCOOPS-isolated RNA in wild-type cells had a wide length distribution that was less prevalent in the HS-deficient mutant (Figure S5A). We took a ligation-based strategy to introduce sequencing adapters so that both polyadenylated and non-polyadenylated RNA biotypes in the sequencing library will be covered (Figure S5B). The reverse-transcribed, PCR-amplified DNA libraries were size-selected (Figure S5C) and, finally, subjected to Illumina platforms for sequencing.

The principal component analysis of sequencing data revealed a large difference between SCOOPS-isolated RNA and the total transcriptome (see Table S5 for a complete read count per million mapped reads [RPM] table) (Figure S5H). Comparing SCOOPS-isolated RNA with total RNA (SCOOPS_WT vs. total_WT) can identify the transcripts that were enriched in the interphase due to crosslinking. These transcripts are colored as yellow dots in the scatterplot (Figure 5A).

We asked if any hepRNA had been retained in the SCOOPS interphase. We define hepRNA as transcripts that are substantially reduced or absent in the SCOOPS interphase of the EXT2-KO mutant (SCOOPS_KO) when compared with those in the wild-type SCOOPS interphase (SCOOPS_WT). As illustrated in the connected boxplot (Figure 5B), of the well-retained transcripts in the SCOOPS_WT interphase (yellow dots in Figure 5A), many had substantially reduced counts in SCOOPS_KO samples. These transcripts include mainly mRNA and long non-coding RNA (lncRNA), which have been major csRNA biotypes in previously reported datasets.[3,4] In particular, metastasis associated lung adenocarcinoma transcript 1 (MALAT1), as one of the few validated cell-surface lncRNA, was also highly enriched in the SCOOPS interphase as hepRNA. The results suggested that SCOOPS effectively captures hepRNA in the interphase.

To comprehensively identify hepRNA candidates, we first normalized the read counts of SCOOPS_WT and SCOOPS_KO on the background RNA species (Figures S5D–S5G; see also method details). It is crucial to note that while SCOOPS is designed to crosslink all RNA-protein complexes at the site of SO generation, it is not specific to hepRNA. The key to ensuring hepRNA specificity was the use of HS-deficient cells as a negative control. In this setup, RNA species that are (1) present at the cell surface but independent of HS or (2) non-specifically crosslinked or isolated during SCOOPS would show minimal

(H) Image and bar graphs of 1% agarose gel electrophoresis of 3′ end Cy5-labeled RNA from wild-type and EXT2-KO (HS-deficient) cells. The wild-type samples were produced in the same batch as EXT2-KO samples. $n = 4$ independent cell cultures. Error bars represent SD.
(I) Bar graphs of flow cytometry quantification of streptavidin-EY recruited on the surface of wild-type cells with or without RNase treatment and EXT2-KO cells. $n = 2$ independent cell cultures. Error bars represent SD.

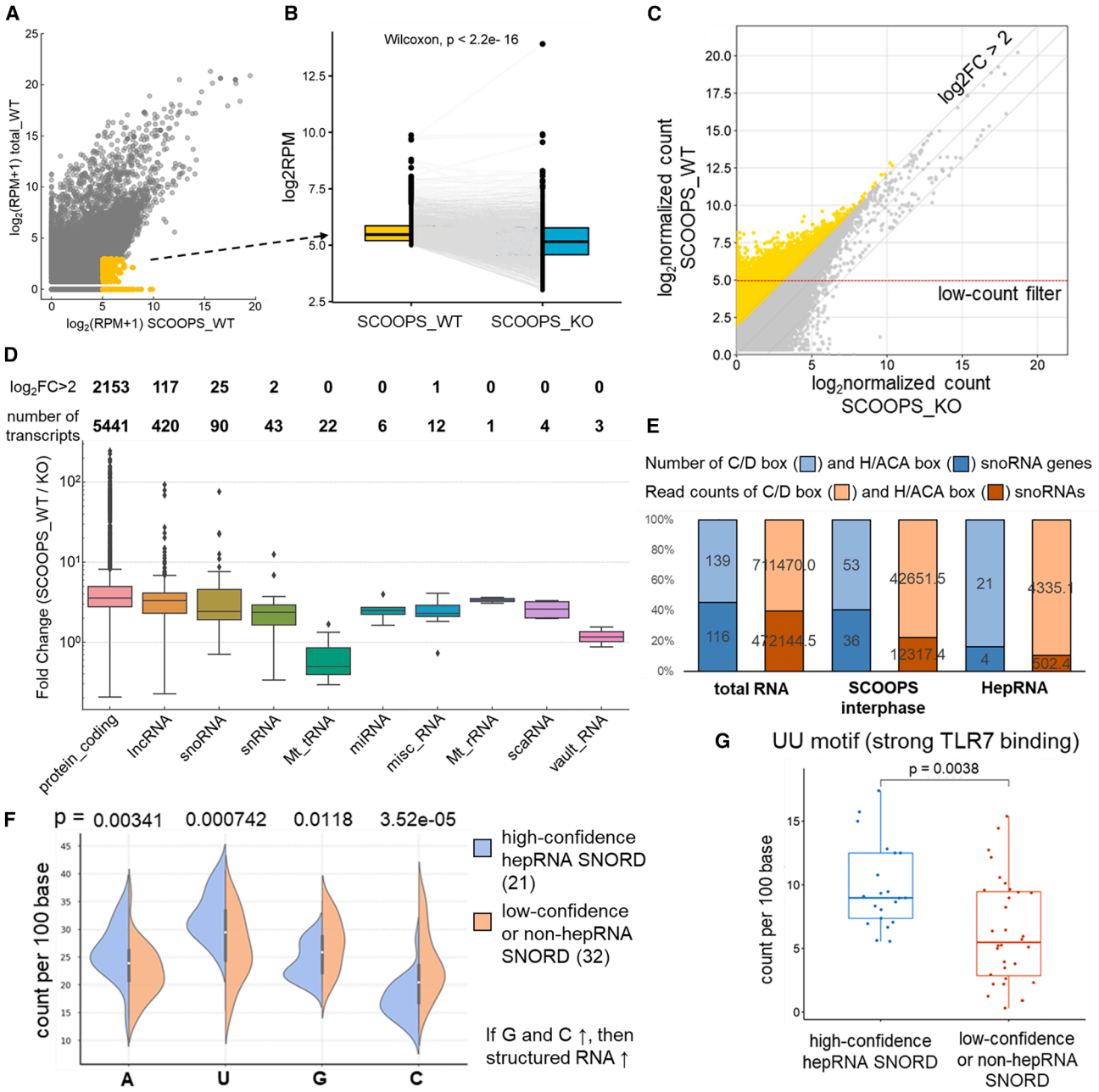

Figure 5. hepRNA identification via next-generation sequencing

(A) Scatterplot of mean RPM values. Mean (RPM + 1) was $\log_2$-transformed. Transcripts are displayed without low-count filtering. *x* axis is SCOOPS_WT sample, and *y* axis is the total cellular RNA from wild-type cells. $n = 2$ independent SCOOPS experiments.

(B) Connected boxplot of RPM of SCOOPS interphase-retained transcripts in wild-type (SCOOPS_WT) and EXT-KO (SCOOPS_KO) samples. Gray lines connect corresponding transcripts in both datasets.

(C) Scatterplot of mean read counts normalized on background RNA species, comparing SCOOPS_WT (*y* axis) with SCOOPS_KO (*x* axis). High-confidence hepRNA (yellow dots) is defined as the transcripts that have 4 times higher read counts post-normalization (on background RNA) in SCOOPS_WT than in SCOOPS_KO. Transcripts with normalized read counts larger than 32 in SCOOPS_WT were taken for further analysis in (D)–(G).

(D) Boxplot summarizing FC values per RNA biotype derived from SCOOPS_WT over _KO. The top of the box represents the 25th percentile, the bottom represents the 75th percentile, the central line indicates the median, the whisker extends to extreme points that are within 1.5× the interquartile range of the box, and individual points beyond whiskers are shown as dots.

(E) Bar graph illustrating relative composition of snoRNA subtypes in total transcriptome, SCOOPS interphase, and as high-confidence hepRNA.

(F) Violin plot showing significant difference in nucleotide compositions between high-confidence hepRNA and low-confidence/non-hepRNA SNORD transcripts.

(G) Boxplot showing strong TLR7-binding motif (UU) occurs more frequently in high-confidence hepRNA SNORD transcripts than in low-confidence/non-hepRNA ones.

enrichment when comparing SCOOPS_WT with SCOOPS_KO datasets.

We applied a FC criteria (FC > 4, SCOOPS_WT over _KO) to classify the hepRNA candidates, indicating that a transcript's presentation on the cell surface is highly dependent on HS. This criterion applies to many mRNA, lncRNA, and small nucleolar RNA (snoRNA) transcripts (Figures 5C and 5D; see Table S6 for a full candidate list). By contrast, transcripts with a lower FC ($2 < FC < 3$) are considered low-confidence hepRNA candidates, as they may associate with HS only partially or could partly result from non-specific crosslinking or isolation during SCOOPS. These transcripts span nearly all investigated biotypes. However, mitochondrial tRNA (Mt_tRNA) and vault RNA are unlikely to be hepRNA, as their transcripts were barely enriched in the SCOOPS_WT vs. SCOOPS_KO comparison.

While mRNA and lncRNA biotypes dominate hepRNA candidates, which is consistent with previous studies, strikingly, snoRNAs also constitute a considerable portion of hepRNA. Among the high-confidence snoRNA-derived hepRNA candidates, the C/D box type snoRNA (SNORD) outnumbers the H/ACA type (SNORA) (21 SNORD vs. 4 SNORA) in transcript count and total read coverage (Figure 5E). Remarkably, we identified defining structural traits that distinguish the high-confidence SNORD hepRNAs (hepSNORDs). The high-confidence hepSNORDs contain significantly less guanosine (G) and cytidine (C) compared with the low-confidence/non-hepSNORDs (Figure 5F). Such nucleotide composition suggests that the high-confidence hepSNORDs may harbor fewer duplex or structured regions intra- or intermolecularly.[49,50] Furthermore, in the high-confidence hepSNORDs, the occurrence of consecutive uridines (UU), a motif known for strong TLR7 binding,[20] is significantly more frequent than low-confidence/non-hepSNORDs (Figure 5G). This observation suggests that specific RNA primary structures underlie the ability of this subset of RNA to associate with cell-surface HS.

hepRNA recruits immune receptors to the cell surface

The vicinity of hepRNA to cell-surface glycoproteins motivated us to explore the possibility that ligands or receptors to these proteins may be regulated by hepRNA. Our hepRNA-proximal datasets harbor many membrane glycoproteins, which were no longer enriched in response to RNase treatment (Figure 6A). In search for an appropriate hit to follow up on from our datasets, we found glycoprotein poliovirus receptor (PVR or CD155) had a decrease of ~28-fold in its intensity in the RNase dataset compared with that in the TLR7 one, suggesting PVR is spatially close to hepRNA. Consistently, in a previous study, the mobility of PVR from cell lysates through a sucrose density gradient dramatically changed upon RNase treatment.[51] Additionally, PVR is documented in RBP2GO database, despite having a low RBP2GO score.[52]

Given the RNA proximity or direct interaction, PVR was thus selected for further investigation. PVR overexpresses in different cancers and can bind to T cell immunoreceptor with immunoglobulin and immunoreceptor tyrosine-based inhibitory motif domain (TIGIT),[53] CD96,[54] and KIR2DL5,[55] all of which are inhibitory receptors able to suppress the killing by T cells or NK cells. PVR also interacts with an activating receptor, CD226.[56] The engagement of PVR with these proteins forms immune checkpoints, and they are thus promising targets for cancer immunotherapy. We have envisioned the possible modes of action of hepRNA on PVR recognition (Figure 6B): (1) hepRNA may sterically hinder the binding, (2) hepRNA may facilitate the binding of specific proteins to PVR by functioning as a co-receptor or by priming PVR for optimal recognition, and finally, (3) hepRNA may be just a bystander and have no effect on binding.

We used flow cytometry to quantify the RNase responsiveness of cell-surface binding by the soluble, Fc-tagged version of ectodomains from the four known PVR-binders with and without RNase pre-treatment (Figure 6C). TIGIT and CD226 exhibited little change in response to RNase treatment, indicating that hepRNA does not modulate their recognition. CD96 did not detectably bind to the cell surface in our experimental settings, suggesting additional factors may be required. KIR2DL5 did show a dramatic reduction in fluorescent signals on the cell surface when live cells were pre-treated with RNase. In line with the genetic screening data, the EXT2 KO mutant cells also exhibited a strong reduction in KIR2DL5 binding but not for CD226 or TIGIT (Figure 6D). Neither the RNase treatment nor EXT2 KO negatively affected cell-surface PVR levels (Figures S6A and S6B), indicating that the decrease in KIR2DL5 binding was due to hepRNA removal rather than an effect on PVR expression. Exogenous RNA added to prior hepRNA-depleted cells restored partly KIR2DL5 binding (Figure S6C), suggesting RNA-KIR2DL5 interaction played an important role in recruiting the latter on the cell surface. To confirm the binding of KIR2DL5 proteins to the cell surface is at least partly dependent on PVR, we generated PVR KO cells using CRISPR-Cas9. Upon treatment with extracellular RNase, the residual KIR2DL5 binding was significantly lower in PVR KO cells than in the wild type (Figure S6D). This indicated that KIR2DL5-PVR interaction accounted for a portion of fluorescence signals detected on the cell surface.

To demonstrate KIR2DL5 binds to hepRNA on living cells, we transiently overexpressed the full-length protein fused with a FLAG tag on wild-type and HS-deficient mutant (pgsD-677) CHO cells (Figure S6E, left). We expect the expression of human KIR2DL5 in such a non-human background should minimize protein-protein interactions. Upon KIR2DL5 overexpression, the cells were exposed to UVC irradiation to crosslink RNA with bound proteins *in situ*. After cell lysis, we performed immunoprecipitation against the FLAG tag to pull down KIR2DL5 and, if any, the crosslinked RNA bound to the protein. The co-precipitated KIR2DL5-bound RNA was enzymatically ligated with biotin at 3′ end on-bead and finally subjected to western blot for the detection of biotin. A strong biotin signal as a smear was found above recombinant FLAG-tagged KIR2DL5 band, suggesting RNA co-precipitation (Figure S6E, right). Such smear disappeared in HS-deficient CHO cells, which indicated an HS dependency of the KIR2DL5-bound RNA. To confirm it was the extracellular domain of KIR2DL5 that mediated RNA binding, we performed *in vitro* assays in which human Fc-fused KIR2DL5 extracellular domain or IgG isotype control was incubated with 3′ end biotinylated total cellular RNA fragments, UVC crosslinked, and subjected to western blot. Strong signal was found only for KIR2DL5 crosslinked with biotinylated RNA, whereas that in the IgG control was hardly detectable (Figure S6F). In addition to experimentally demonstrating that hepRNA can interact with KIR2DL5's extracellular

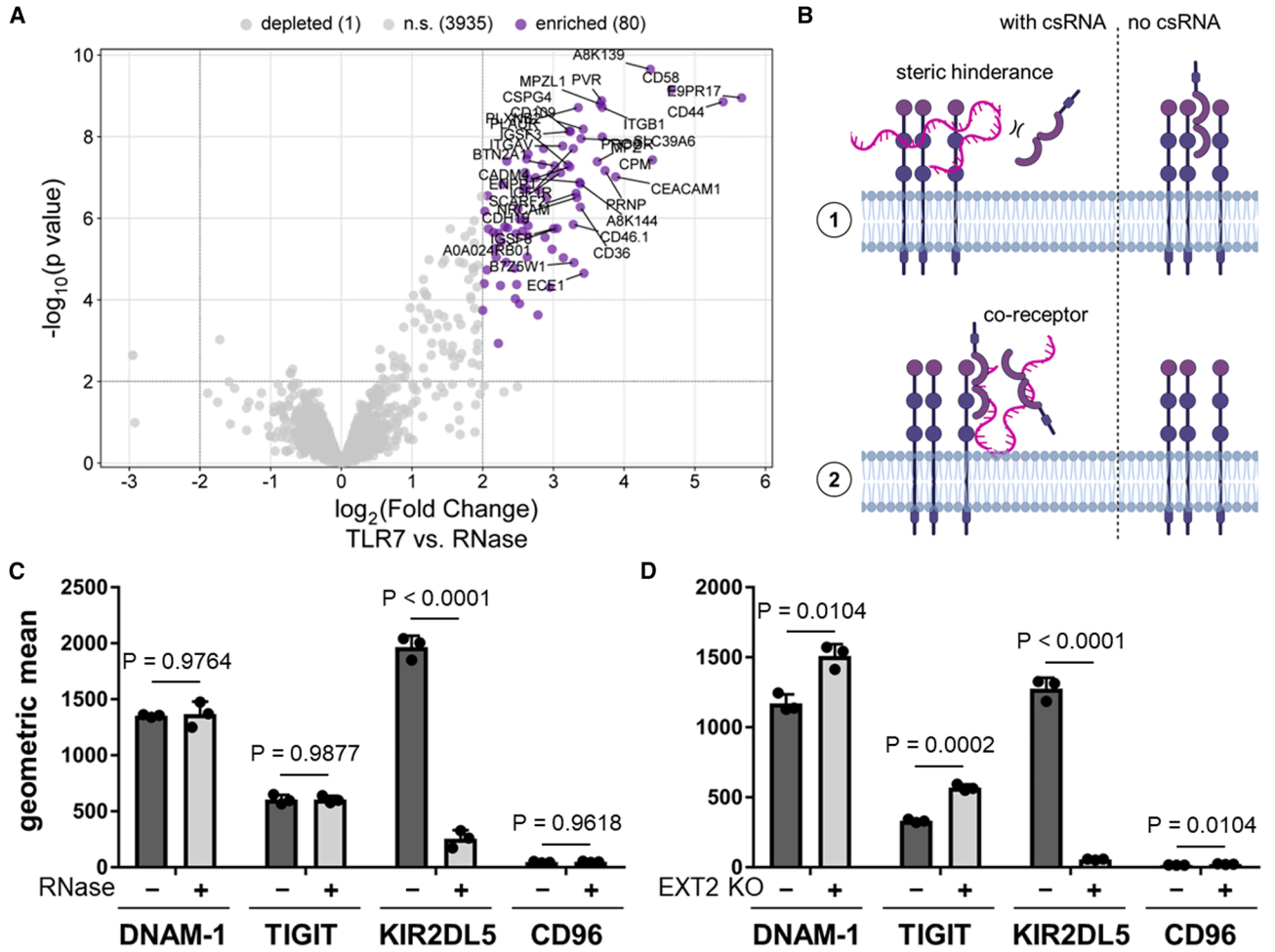

Figure 6. hepRNA recruits KIR2DL5 on the cell surface

(A) Volcano plot from the comparison of proteomes between TLR7-mediated proximity labeling with vs. without RNase treatment. Significantly enriched proteins with high FC (≥ 8, $p < 0.01$) are labeled with their names. $n = 3$ independent cell cultures.

(B) Schematic representation of how csRNA may regulate ligand-receptor interactions on the plasma membrane.

(C) Bar graphs from flow cytometry analysis of live-cell surface binding of PVR-binding Fc-fused recombinant proteins, in the presence or absence of csRNA. 40 μg/mL RNase A was used to deplete csRNA. Alexa Fluor 647-conjugated goat-anti-human was used to detect Fc-fused proteins on the live-cell surface. $n = 3$ independent cell cultures. Error bars represent SD.

(D) Bar graphs from flow cytometry analysis of live-cell surface binding of PVR-binding Fc-fused recombinant proteins. Wild-type Mel526 and the EXT-KO mutant cells were compared side-by-side. $n = 3$ independent cell cultures. Error bars represent SD.

domain, we also postulated a structural model for the interaction using AlphaFold 3 (AF3)[57] (Figures S6G–S6N).

Taken together, these results demonstrate that hepRNA alone can recruit KIR2DL5 on the cell surface, whereas PVR alone only weakly binds to soluble KIR2DL5. The data support the model that hepRNA functions as a co-receptor for KIR2DL5 and thereby facilitates its engagement with PVR by increasing local KIR2DL5 concentration at the cell surface.

DISCUSSION

A hepRNA-csRBP-HS ternary complex model

Taking integrated omic-wide approaches and using multiple orthogonal validatory methods, our study provided insights into how the biomacromolecule is associated with the plasma membrane. The study was commenced by an exploitation of nature's own RNA sensor, TLR7, as a probe to detect RNA at the. The use thereof in a genome-wide CRISPR-Cas9 KO screening led to the discovery of HS polysaccharide as an essential molecular factor for RNA's association with the cell surface. While direct interactions between carbohydrates and nucleic acids have been reported,[58] our data support the presence of a number of RBPs at the cell surface as crucial adapter molecules to bridge the two highly negatively charged biopolymers, forming hepRNA-csRBP-HS ternary complexes (Figure 7).

In addition to the routine validatory experiments, such as immunofluorescence, flow cytometry, and western blot assays, we have established multiple orthogonal methods to validate

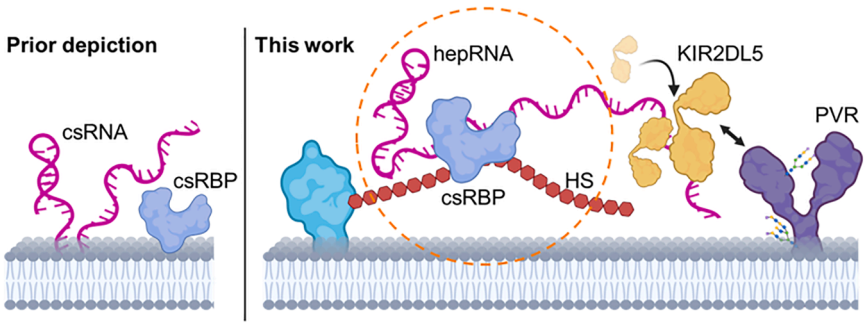

Figure 7. Molecular model of RNA cell-surface presentation
The hepRNA-csRBP-HS ternary complex model is shown in dashed orange circle.

such ternary molecular configuration. We considered that the csRBPs had been an essential element collectively for RNA's association with HS but functionally redundant as individual proteins, particularly as none of the csRBPs from the proteomics study were hits in the genetic screening. This was because the KO of one RBP during the pooled screening may have been compensated by others, such that little, if any, apparent decrease of global hepRNA could be observed in flow cytometry using the TLR7 probe. Due to this collectively essential but individually redundant nature of csRBPs for hepRNA, knocking out these RBPs altogether until a global reduction in hepRNA is seen would be experimentally impractical. We, therefore, opted for an orthogonal approach that works on global csRBPs to validate TLR7-based findings.

We introduced SCOOPS, a crosslinking- and phase partition-based technology to selectively capture cell-surface RNA-protein complexes. It is important to note that the AGPC condition during phase separation is highly denaturing, such that most non-covalent RNA-protein complexes will fall apart and enter aqueous (RNA) and organic (protein) phases. By contrast, the crosslinked RNA-protein complexes are unbreakable by AGPC and are retained in the interphase due to their amphiphilic nature. The significantly more interphase RNA from cell-surface crosslinked wild-type cells compared with the negative controls indicates csRNA had been crosslinked to csRBPs. Likewise, the substantially decreased interphase RNA from HS-deficient cells suggests a reduction of RNA-protein complexes presented on the cell surface. Taken together, SCOOPS served to provide an orthogonal validation, strengthening the ternary complex model.

Furthermore, SCOOPS enabled unveiling the identities of hepRNA. It revealed that decreased G and C content and a more frequent UU motif occurrence are traits in the RNA primary structure related to HS association. Apart from sequence motifs, more factors such as their secondary and higher-order structures and the transcript-specific interacting proteome should be examined,[59] and how they function in an intertwined manner to regulate RNA cell-surface localization remains to be elucidated.[60]

While our data support a ternary complex model of hepRNA-csRBP-HS, the structural basis for the interaction between RBPs and HS remains elusive. Thus, future work will be needed on investigating the molecular details of how RBPs bind to HS. HS is known to be a molecular mimicry of nucleic acids, and there have been reports showing several nucleic acid-binding proteins can indeed interact with HS. Generally, the interaction between RBP and HS may be mediated by a designated HS-binding domain present on the RBP or a promiscuous RNA-binding domain,[61] which typically harbors positively charged side chains for the electrostatic interaction with HS. SSB, for example, contains a putative HS-binding motif (GRRFKG) at its C terminus disordered region, implying potential HS-binding activity.[62] Conversely, HNRNPA1 does not contain any known HS-binding motif, despite its presence on the cell surface of wild-type but not on HS-deficient mutant cells. It suggests a yet-to-be-characterized mode of interaction between HS and the RNA-binding domains or other portions of the protein.

hepRNA as a co-binder for KIR2DL5

We further demonstrate that once displayed on the cell surface, the RNA can enrich glycoprotein immune receptors, likely to facilitate the interaction with their cognate ligands. In the case of KIR2DL5, hepRNA functions as a co-binder, such that the local concentration of KIR2DL5 becomes much higher, thereby facilitating PVR engagement and compensating for the weak affinity of PVR for KIR2DL5.[55] The co-binder effect in modulating cell-surface receptor-ligand interactions is not uncommon. For example, the engagement of FGF-2 with FGF receptor (FGFR) requires the former to engage with HS, likely resulting in a liquid-liquid phase separation.[63]

KIR2DL5, together with a few other KIR family members, has been previously shown to bind to heparin *in vitro* via the d0 domain, which is rich in positively charged amino acids.[64] Heparin is often considered a molecular mimicry of nucleic acids because of its heavy negative charges along the polysaccharide chain and has been used to purify select nucleic acid-binding proteins. Although binding to heparin *in vitro*, we demonstrated that KIR2DL5 could directly bind to RNA *in vitro* and, at least partly, on living cell surface, for which a structural basis was predicted using AF3. Notably, such promiscuity in binding has been described for a cell-surface-localized protein, receptor for advanced glycation end products (RAGE). It was shown previously to bind to HS[65] and more recently also to DNA.[66] Similar observation has also been made for certain antibodies directed against DNA, which can cross-react with HS.[67,68]

Origin of hepRNA

One key question remains as to the origin of the hepRNA and the associated csRBPs. It is plausible that the RNPs are transported from the cytosol to the plasma membrane of the same cell ("inside-out"). However, the inside-out model requires the translocation of cytosolic RNA and RBPs to the luminal side of specific membranous organelles. Interestingly, a recent study[69] showed a distinct set of RNAs from the cytosolically localized transcripts can be found in the endoplasmic reticulum (ER) lumen, implying

an unidentified pathway for RNA luminal translocation. In our genetic screening study, TMED10 was identified as an essential factor for hepRNA presentation. This multifunctional protein forms channels on the ER-Golgi Intermediate Compartment (ERGIC) membrane and mediates the translocation of select cytosolic proteins without leader peptides to the luminal side for secretion.[70] Of particular interest, TMED10 was reportedly not relevant to HS biosynthesis[71] and has been documented to potentially bind to RNA in the RBP2GO database,[52] implicating their possible roles in vesicular RNA transport.

An equally likely scenario would be that they are secreted from live cells or released from dead/dying cells and directly deposited on the HS chains (“outside-on”). There are numerous biological processes in which intracellular components, including RNA (protein unbound or in complex), are released to extracellular space. The release can be from not only dying/dead cells or damaged tissues but also living cells.[72] Extracellular RNAs or their protein complexes are common damage-associated molecular patterns (DAMPs), which can activate innate and adaptive immunity and are associated with many disorders,[73] such as sepsis,[74] cancer,[75] and autoimmune diseases.[76] The observation that HS, but not other proteoglycans, can selectively capture extracellular RNA-protein complexes is strong evidence of a specific and biologically relevant interaction, suggesting that HS plays a unique role in regulating extracellular RNA dynamics and immune activation. On the one hand, it may limit RNA-based DAMPs locally by capturing them to slow down their lateral diffusion. On the other hand, it may also serve as a scaffold to present the RNPs to immune cells for activation. Further exploration of HS-RBP-RNA interactions could uncover novel regulators of immune signaling in tissue injury, offering new insights into inflammation-related diseases.

Limitations of the study

In this work, we establish a foundational model for the ternary association among HS, RNA, and RBP at the mammalian cell surface. Key to this model was the use of the recombinant TLR7 as a probe for detecting csRNA on living cells. While demonstrated to bind to total RNA fragments *in vitro* herein, it remains unclear how the TLR7 ectodomain interacts with csRNA, especially as the protein employs two distinct sites for sensing RNA and/or its degradation products. Future studies will focus on a more detailed characterization at the molecular level of the functional binding site in TLR7 for csRNA recognition.

In the genetic screening studies, while we validated a few essential factors for csRNA presentation identified from the $TLR7^{low}$ population, we did not follow up on the hits from the $TLR7^{high}$ population, which should in principle contain factors limiting csRNA presentation. However, the relevance of CMAS, UROD, or CLEC17A to csRNA remains clear. Future studies may investigate further potential cellular factors associated with csRNA turnover.

In the RNA sequencing studies, although our sequence and motif analyses indicate uridine enrichment and diminished GC content as potential characteristics of hepRNAs, the extensive variety of RNA secondary structures and their role in csRNA presentation have yet to be investigated. TLR7’s binding specificity for exclusively single-stranded RNAs implies that csRNA may contain substantial single-stranded regions. However, the true conformation of RNA at the cell surface, whether it differs from the intracellular RNAs, and how their structures influence csRNA functions remain to be elucidated.

Finally, although our data indicate a possible immunomodulatory function for hepRNA through the recruitment of KIR2DL5, the physiological significance of these complexes remains to be verified.

RESOURCE AVAILABILITY

Lead contact

Requests for further information and resources should be directed to and will be fulfilled by the lead contact, Zeshi Li (z.li@uu.nl).

Materials availability

All reagents generated in this study will be made available on request from the lead contact with a completed materials transfer agreement.

Data and code availability

- The genetic screening data in fastq format are deposited in the European Nucleotide Archive and are publicly accessible with the project accession code ENA: PRJEB88327. Proteomics data are deposited in the PRIDE Partner Repository with the identifier PRIDE: PXD061693. The RNA sequencing data in the fastq format from SCOOPS experiments are deposited in the European Nucleotide Archive and are publicly accessible with the project accession code ENA: PRJEB88260.
- This study does not report any original software code.
- The unprocessed/uncropped images of gels and blots and immunofluorescence have been deposited in Mendeley Data and are publicly accessible via DOI: https://doi.org/10.17632/sjrv6wm5dh.1.
- Any additional information required to reanalyze the data reported in this paper is also available from the lead contact upon request.

ACKNOWLEDGMENTS

T.H.S., V.R., and C.J. were supported by the TU Delft-Leiden Health Initiative. C.J. was supported by the ERC Consolidator grant (819299) of the European Research Council, the Ministry of Science and ICT (Bio&Medical Technology Development Program of the National Research Foundation, RS-2025-02217909; the Basic Research Laboratory Program, NRF-2023R1A2C2004745), and Frontier 10-10 (Ewha Woman’s University). Z.L. was supported by the NWO Veni talent program (VI.Veni.222.272). H.Y. is supported by the Chinese Scholarship Council (202308320069). V.R. and Z.L. were supported by Human Genetics NGS Pilot Project Funding (Leiden University Medical Center, the Netherlands). M.V. is part of the Oncode Institute, which is partly funded by the Dutch Cancer Society (KWF).The proteomics research and associated analyses reported in this publication was supported by Oncode Accelerator, a Dutch National Growth Fund project under grant number NGFOP2201. We thank Geert-Jan Boons (Utrecht University, the Netherlands, and University of Georgia, USA) for critical discussion, Abhijeet Pataskar (NKI, the Netherlands) for helping with RNA sequencing data analysis, Kelly Stecker (Utrecht University), Daniel Peeper (NKI, the Netherlands), and Sjaak Neefjes (Leiden University) for providing important resources.

AUTHOR CONTRIBUTIONS

Z.L., C.J., and V.R. conceived the study. C.J., Z.L., and V.R. jointly supervised the studies. Z.L. performed flow cytometry, UV crosslinking, and immunoprecipitation of RNA experiments. B.S.J. performed immunofluorescence imaging experiments. B.S.J., E.B., and T.H.S. performed EM imaging. Z.L. and R.H.W. performed genome-wide screening. R.H.W. processed and analyzed deep sequencing data. R.H.W. and B.S.J. produced heparan sulfate-deficient mutant cells. Z.L. and I.S.-B. performed TLR7-Fc-proximity biotinylation experiments. H.Y. performed surface biotinylation and OOPS experiments.

D.W.Z. and I.S.-B. performed LC-MS sample preparation. Z.L., D.W.Z., and I.S.-B. performed proteomics data processing and analysis. H.Y. and A.K. developed photo-crosslinking and SCOOPS technologies. M.S. produced PVR-knockout mutant cells. W.W. and F.M.Z. performed KIR2DL5-RNA coIP. P.C. performed SPR. M.V. supervised the proteomics study. Z.L., H.M., and V.R. analyzed RNA sequencing data. M.E.T. provided critical input and suggested useful resources for the study. Z.L., B.S.J., V.R., and C.J. co-wrote the manuscript with input from all authors.

DECLARATION OF INTERESTS

I.S.-B. (former post-doctoral researcher at M.V. lab) is a product developer at Solvias NL.

STAR★METHODS

Detailed methods are provided in the online version of this paper and include the following:

- KEY RESOURCES TABLE
- EXPERIMENTAL MODEL AND STUDY PARTICIPANT DETAILS
  - Cell culture
- METHOD DETAILS
  - Immunocytochemistry
  - Electron microscopy
  - Flow cytometry analysis of csRNA on live cells
  - TLR7-Fc binding rescue by exogenous RNA
  - TLR7-RNA crosslinking, precipitation, and on-bead RNA labelling
  - Proximity biotinylation of csRNA-proximal proteome
  - Proteomics sample preparation and LC-MS/MS analysis
  - Proteomics data analysis
  - Genetic screening and data analysis
  - Genetic screening hit validation
  - Preparation of PVR KO mutant cells
  - UVC and eosin Y-mediated crosslinking and orthogonal organic phase separation (OOPS)
  - Conjugation of eosin isothiocyanate to streptavidin
  - Enzyme-linked immunosorbent assay (ELISA) of EY-conjugated streptavidin
  - Spatio-selective crosslinking followed by OOPS (SCOOPS)
  - RNA sequencing library preparation
  - Sequencing data analysis
  - Read count normalization on background RNA species
  - KIR2DL5 transfection, in-situ crosslinking and RNA co-precipitation
  - Biotinylation at total RNA fragments 3'-end (for *in vitro* KIR2DL5 binding)
  - *In vitro* KIR2DL5 binding, crosslinking, and RNA co-precipitation
  - AlphaFold3 prediction of structural model for KIR2DL5 and potential interacting partners
- QUANTIFICATION AND STATISTICAL ANALYSIS

SUPPLEMENTAL INFORMATION

Supplemental information can be found online at https://doi.org/10.1016/j.molcel.2025.11.020.

Received: July 1, 2024
Revised: July 16, 2025
Accepted: November 18, 2025
Published: December 18, 2025

REFERENCES

1. Block, K.F., Puerta-Fernandez, E., Wallace, J.G., and Breaker, R.R. (2011). Association of OLE RNA with bacterial membranes via an RNA-protein interaction. Mol. Microbiol. *79*, 21–34. https://doi.org/10.1111/j.1365-2958.2010.07439.x.
2. Flynn, R.A., Pedram, K., Malaker, S.A., Batista, P.J., Smith, B.A.H., Johnson, A.G., George, B.M., Majzoub, K., Villalta, P.W., Carette, J.E., et al. (2021). Small RNAs are modified with *N*-glycans and displayed on the surface of living cells. Cell *184*, 3109–3124.e22. https://doi.org/10.1016/j.cell.2021.04.023.
3. Huang, N., Fan, X., Zaleta-Rivera, K., Nguyen, T.C., Zhou, J., Luo, Y., Gao, J., Fang, R.H., Yan, Z., Chen, Z.B., et al. (2020). Natural display of nuclear-encoded RNA on the cell surface and its impact on cell interaction. Genome Biol. *21*, 225. https://doi.org/10.1186/s13059-020-02145-6.
4. Wu, E., Guo, X., Teng, X., Zhang, R., Li, F., Cui, Y., Zhang, D., Liu, Q., Luo, J., Wang, J., et al. (2021). Discovery of Plasma Membrane-Associated RNAs through APEX-seq. Cell Biochem. Biophys. *79*, 905–917. https://doi.org/10.1007/s12013-021-00991-0.
5. Hemberger, H., Chai, P., Lebedenko, C.G., Caldwell, R.M., George, B.M., and Flynn, R.A. (2023). Rapid and sensitive detection of native glycoRNAs. Preprint at bioRxiv.
6. Zhang, N., Tang, W., Torres, L., Wang, X., Ajaj, Y., Zhu, L., Luan, Y., Zhou, H., Wang, Y., Zhang, D., et al. (2024). Cell surface RNAs control neutrophil recruitment. Cell *187*, 846–860.e17. https://doi.org/10.1016/j.cell.2023.12.033.
7. Semenkovich, C.F., Ostlund, R.E., Jr., Olson, M.O., and Yang, J.W. (1990). A protein partially expressed on the surface of HepG2 cells that binds lipoproteins specifically is nucleolin. Biochemistry *29*, 9708–9713. https://doi.org/10.1021/bi00493a028.
8. Jo, S.H., Choi, J.-A., Lim, Y.-J., Lee, J., Cho, S.-N., Oh, S.-M., Go, D., Kim, S.-H., and Song, C.-H. (2017). Calreticulin modulates the intracellular survival of mycobacteria by regulating ER-stress-mediated apoptosis. Oncotarget *8*, 58686–58698. https://doi.org/10.18632/oncotarget.17419.
9. Knorr, K., Rahman, J., Erickson, C., Wang, E., Monetti, M., Li, Z., Ortiz-Pacheco, J., Jones, A., Lu, S.X., Stanley, R.F., et al. (2023). Systematic evaluation of AML-associated antigens identifies anti-U5 SNRNP200 therapeutic antibodies for the treatment of acute myeloid leukemia. Nat. Cancer *4*, 1675–1692. https://doi.org/10.1038/s43018-023-00656-2.
10. Gillissen, M.A., Kedde, M., Jong, G., Gillissen, M.A., Kedde, M., Jong, G., Moiset, G., Yasuda, E., Levie, S.E., Bakker, A.Q., Claassen, Y.B., Wagner, K., Böhne, M., et al. (2018). AML-specific cytotoxic antibodies in patients with durable graft-versus-leukemia responses. Blood *131*, 131–143. https://doi.org/10.1182/blood-2017-02-768762.
11. Perr, J., Langen, A., Almahayni, K., Nestola, G., Chai, P., Lebedenko, C.G., Volk, R.F., Detrés, D., Caldwell, R.M., Spiekermann, M., et al. (2025). RNA-binding proteins and glycoRNAs form domains on the cell surface for cell-penetrating peptide entry. Cell *188*, 1878–1895.e25. https://doi.org/10.1016/j.cell.2025.01.040.
12. Vallet, S.D., Clerc, O., and Ricard-Blum, S. (2020). Glycosaminoglycan–Protein Interactions: The First Draft of the Glycosaminoglycan Interactome. J. Histochem. Cytochem. *69*, 93–104. https://doi.org/10.1369/0022155420946403.
13. Esko, J.D., and Lindahl, U. (2001). Molecular diversity of heparan sulfate. J. Clin. Investig. *108*, 169–173. https://doi.org/10.1172/JCI13530.
14. Lamanna, W.C., Kalus, I., Padva, M., Baldwin, R.J., Merry, C.L.R., and Dierks, T. (2007). The heparanome—The enigma of encoding and decoding heparan sulfate sulfation. J. Biotechnol. *129*, 290–307. https://doi.org/10.1016/j.jbiotec.2007.01.022.
15. Ma, Y., Guo, W., Mou, Q., Shao, X., Lyu, M., Garcia, V., Kong, L., Lewis, W., Ward, C., Yang, Z., et al. (2024). Spatial imaging of glycoRNA in single cells with ARPLA. Nat. Biotechnol. *42*, 608–616. https://doi.org/10.1038/s41587-023-01801-z.
16. Petes, C., Odoardi, N., and Gee, K. (2017). The Toll for Trafficking: Toll-Like Receptor 7 Delivery to the Endosome. Front. Immunol. *8*, 1075. https://doi.org/10.3389/fimmu.2017.01075.
17. Crawford, J.D., Wang, H., Trejo-Zambrano, D., Cimbro, R., Talbot, C.C., Jr., Thomas, M.A., Curran, A.M., Girgis, A.A., Schroeder, J.T., Fava, A.,

et al. (2023). The XIST lncRNA is a sex-specific reservoir of TLR7 ligands in SLE. JCI Insight *8*, e169344. https://doi.org/10.1172/jci.insight.169344.

18. Lehmann, S.M., Krüger, C., Park, B., Derkow, K., Rosenberger, K., Baumgart, J., Trimbuch, T., Eom, G., Hinz, M., Kaul, D., et al. (2012). An unconventional role for miRNA: let-7 activates Toll-like receptor 7 and causes neurodegeneration. Nat. Neurosci. *15*, 827–835. https://doi.org/10.1038/nn.3113.

19. Pawar, K., Shigematsu, M., Sharbati, S., and Kirino, Y. (2020). Infection-induced 5′-half molecules of tRNAHisGUG activate Toll-like receptor 7. PLoS Biol. *18*, e3000982. https://doi.org/10.1371/journal.pbio.3000982.

20. Zhang, Z., Ohto, U., Shibata, T., Taoka, M., Yamauchi, Y., Sato, R., Shukla, N.M., David, S.A., Isobe, T., Miyake, K., et al. (2018). Structural Analyses of Toll-like Receptor 7 Reveal Detailed RNA Sequence Specificity and Recognition Mechanism of Agonistic Ligands. Cell Rep. *25*, 3371–3381.e5. https://doi.org/10.1016/j.celrep.2018.11.081.

21. Monsigny, M., Roche, A.C., Sene, C., Maget-Dana, R., and Delmotte, F. (1980). Sugar-Lectin Interactions: How Does Wheat-Germ Agglutinin Bind Sialoglycoconjugates? Eur. J. Biochem. *104*, 147–153. https://doi.org/10.1111/j.1432-1033.1980.tb04410.x.

22. Fischer, L.S., Klingner, C., Schlichthaerle, T., Strauss, M.T., Böttcher, R., Fässler, R., Jungmann, R., and Grashoff, C. (2021). Quantitative single-protein imaging reveals molecular complex formation of integrin, talin, and kindlin during cell adhesion. Nat. Commun. *12*, 919. https://doi.org/10.1038/s41467-021-21142-2.

23. Owen, D.M., Rentero, C., Rossy, J., Magenau, A., Williamson, D., Rodriguez, M., and Gaus, K. (2010). PALM imaging and cluster analysis of protein heterogeneity at the cell surface. J. Biophotonics *3*, 446–454. https://doi.org/10.1002/jbio.200900089.

24. Melan, M.A., and Sluder, G. (1992). Redistribution and differential extraction of soluble proteins in permeabilized cultured cells. Implications for immunofluorescence microscopy. J. Cell Sci. *101*, 731–743. https://doi.org/10.1242/jcs.101.4.731.

25. Tanaka, K.A.K., Suzuki, K.G.N., Shirai, Y.M., Shibutani, S.T., Miyahara, M.S.H., Tsuboi, H., Yahara, M., Yoshimura, A., Mayor, S., Fujiwara, T.K., et al. (2010). Membrane molecules mobile even after chemical fixation. Nat. Methods *7*, 865–866. https://doi.org/10.1038/nmeth.f.314.

26. Helmreich, E.J.M. (2003). Environmental influences on signal transduction through membranes: a retrospective mini-review. Biophys. Chem. *100*, 519–534. https://doi.org/10.1016/S0301-4622(02)00303-4.

27. Dhir, A., Dhir, S., Borowski, L.S., Jimenez, L., Teitell, M., Rötig, A., Crow, Y.J., Rice, G.I., Duffy, D., Tamby, C., et al. (2018). Mitochondrial double-stranded RNA triggers antiviral signalling in humans. Nature *560*, 238–242. https://doi.org/10.1038/s41586-018-0363-0.

28. Weber, F., Wagner, V., Rasmussen, S.B., Hartmann, R., and Paludan, S.R. (2006). Double-Stranded RNA Is Produced by Positive-Strand RNA Viruses and DNA Viruses but Not in Detectable Amounts by Negative-Strand RNA Viruses. J. Virol. *80*, 5059–5064. https://doi.org/10.1128/JVI.80.10.5059-5064.2006.

29. Van Nostrand, E.L., Pratt, G.A., Shishkin, A.A., Gelboin-Burkhart, C., Fang, M.Y., Sundararaman, B., Blue, S.M., Nguyen, T.B., Surka, C., Elkins, K., et al. (2016). Robust transcriptome-wide discovery of RNA-binding protein binding sites with enhanced CLIP (eCLIP). Nat. Methods *13*, 508–514. https://doi.org/10.1038/nmeth.3810.

30. Sanson, K.R., Hanna, R.E., Hegde, M., Donovan, K.F., Strand, C., Sullender, M.E., Vaimberg, E.W., Goodale, A., Root, D.E., Piccioni, F., et al. (2018). Optimized libraries for CRISPR-Cas9 genetic screens with multiple modalities. Nat. Commun. *9*, 5416. https://doi.org/10.1038/s41467-018-07901-8.

31. Marques, C., Reis, C.A., Vivès, R.R., and Magalhães, A. (2021). Heparan Sulfate Biosynthesis and Sulfation Profiles as Modulators of Cancer Signalling and Progression. Front. Oncol. *11*, 778752. https://doi.org/10.3389/fonc.2021.778752.

32. Kamiyama, S., Suda, T., Ueda, R., Suzuki, M., Okubo, R., Kikuchi, N., Chiba, Y., Goto, S., Toyoda, H., Saigo, K., et al. (2003). Molecular Cloning and Identification of 3′-Phosphoadenosine 5′-Phosphosulfate Transporter. J. Biol. Chem. *278*, 25958–25963. https://doi.org/10.1074/jbc.M302439200.

33. Durin, Z., Dubail, J., Layotte, A., Legrand, D., Cormier-Daire, V., and Foulquier, F. (2022). SLC10A7, an orphan member of the SLC10 family involved in congenital disorders of glycosylation. Hum. Genet. *141*, 1287–1298. https://doi.org/10.1007/s00439-021-02420-x.

34. Vanderperre, B., Muraleedharan, A., Dorion, M.F., Larroquette, F., Del Cid Pellitero, E., Rajakulendran, N., Chen, C.X.Q., Larivière, R., Michaud-Tardif, C., Chidiac, R., et al. (2023). A genome-wide CRISPR/Cas9 screen identifies genes that regulate the cellular uptake of α-synuclein fibrils by modulating heparan sulfate proteoglycans. Preprint at bioRxiv.

35. van den Born, J., Salmivirta, K., Henttinen, T., Östman, N., Ishimaru, T., Miyaura, S., Yoshida, K., and Salmivirta, M. (2005). Novel Heparan Sulfate Structures Revealed by Monoclonal Antibodies. J. Biol. Chem. *280*, 20516–20523. https://doi.org/10.1074/jbc.M502065200.

36. Li, J., Han, S., Li, H., Udeshi, N.D., Svinkina, T., Mani, D.R., Xu, C., Guajardo, R., Xie, Q., Li, T., et al. (2020). Cell-Surface Proteomic Profiling in the Fly Brain Uncovers Wiring Regulators. Cell *180*, 373–386.e15. https://doi.org/10.1016/j.cell.2019.12.029.

37. Yang, Z., Zhang, Y., Fang, Y., Zhang, Y., Du, J., Shen, X., Zhang, K., Zou, P., and Chen, Z. (2024). Spatially barcoding biochemical reactions using DNA nanostructures unveil a major contact mechanism in proximity labeling. Preprint at bioRxiv. https://doi.org/10.1101/2024.12.17.628942.

38. Oakley, J.V., Buksh, B.F., Fernández, D.F., Oblinsky, D.G., Seath, C.P., Geri, J.B., Scholes, G.D., and MacMillan, D.W.C. (2022). Radius measurement via super-resolution microscopy enables the development of a variable radii proximity labeling platform. Proc. Natl. Acad. Sci. USA *119*, e2203027119. https://doi.org/10.1073/pnas.2203027119.

39. König, J., Zarnack, K., Rot, G., Curk, T., Kayikci, M., Zupan, B., Turner, D.J., Luscombe, N.M., and Ule, J. (2010). iCLIP reveals the function of hnRNP particles in splicing at individual nucleotide resolution. Nat. Struct. Mol. Biol. *17*, 909–915. https://doi.org/10.1038/nsmb.1838.

40. Huppertz, I., Perez-Perri, J.I., Mantas, P., Sekaran, T., Schwarzl, T., Russo, F., Ferring-Appel, D., Koskova, Z., Dimitrova-Paternoga, L., Kafkia, E., et al. (2022). Riboregulation of Enolase 1 activity controls glycolysis and embryonic stem cell differentiation. Mol. Cell *82*, 2666–2680.e11. https://doi.org/10.1016/j.molcel.2022.05.019.

41. Timchenko, L.T., Iakova, P., Welm, A.L., Cai, Z.J., and Timchenko, N.A. (2002). Calreticulin Interacts with C/EBPalpha and C/EBPbeta mRNAs and Represses Translation of C/EBP Proteins. Mol. Cell. Biol. *22*, 7242–7257. https://doi.org/10.1128/MCB.22.20.7242-7257.2002.

42. Koh, E., and Fluhr, R. (2016). Singlet oxygen detection in biological systems: Uses and limitations. Plant Signal. Behav. *11*, e1192742. https://doi.org/10.1080/15592324.2016.1192742.

43. Luo, H., Tang, W., Liu, H., Zeng, X., Ngai, W.S.C., Gao, R., Li, H., Li, R., Zheng, H., and Guo, J. (2022). Photocatalytic Chemical Crosslinking for Profiling RNA–Protein Interactions in Living Cells. Angew. Chem. Intl. Ed. *61*, e202202008. https://doi.org/10.1002/anie.202202008.

44. Lin, Z., Schaefer, K., Lui, I., Yao, Z., Fossati, A., Swaney, D.L., Palar, A., Sali, A., and Wells, J.A. (2024). Multiscale photocatalytic proximity labeling reveals cell surface neighbors on and between cells. Science *385*, eadl5763. https://doi.org/10.1126/science.adl5763.

45. Müller, M., Gräbnitz, F., Barandun, N., Shen, Y., Wendt, F., Steiner, S.N., Severin, Y., Vetterli, S.U., Mondal, M., Prudent, J.R., et al. (2021). Light-mediated discovery of surfaceome nanoscale organization and intercellular receptor interaction networks. Nat. Commun. *12*, 7036. https://doi.org/10.1038/s41467-021-27280-x.

46. Queiroz, R.M.L., Smith, T., Villanueva, E., Marti-Solano, M., Monti, M., Pizzinga, M., Mirea, D.-M., Ramakrishna, M., Harvey, R.F., Dezi, V., et al. (2019). Comprehensive identification of RNA–protein interactions in

any organism using orthogonal organic phase separation (OOPS). Nat. Biotechnol. *37*, 169–178. https://doi.org/10.1038/s41587-018-0001-2.

47. Trendel, J., Schwarzl, T., Horos, R., Prakash, A., Bateman, A., Hentze, M.W., and Krijgsveld, J. (2019). The Human RNA-Binding Proteome and Its Dynamics during Translational Arrest. Cell *176*, 391–403.e19. https://doi.org/10.1016/j.cell.2018.11.004.
48. Urdaneta, E.C., Vieira-Vieira, C.H., Hick, T., Wessels, H.-H., Figini, D., Moschall, R., Medenbach, J., Ohler, U., Granneman, S., Selbach, M., et al. (2019). Purification of cross-linked RNA-protein complexes by phenol-toluol extraction. Nat. Commun. *10*, 990. https://doi.org/10.1038/s41467-019-08942-3.
49. Chan, C.Y., Carmack, C.S., Long, D.D., Maliyekkel, A., Shao, Y., Roninson, I.B., and Ding, Y. (2009). A structural interpretation of the effect of GC-content on efficiency of RNA interference. BMC Bioinform. *10*, S33. https://doi.org/10.1186/1471-2105-10-S1-S33.
50. Zhang, J., Kuo, C.C.J., and Chen, L. (2011). GC content around splice sites affects splicing through pre-mRNA secondary structures. BMC Genomics *12*, 90. https://doi.org/10.1186/1471-2164-12-90.
51. Caudron-Herger, M., Rusin, S.F., Adamo, M.E., Seiler, J., Schmid, V.K., Barreau, E., Kettenbach, A.N., and Diederichs, S. (2019). R-DeeP: Proteome-wide and Quantitative Identification of RNA-Dependent Proteins by Density Gradient Ultracentrifugation. Mol. Cell *75*, 184–199.e10. https://doi.org/10.1016/j.molcel.2019.04.018.
52. Caudron-Herger, M., Jansen, R.E., Wassmer, E., and Diederichs, S. (2021). RBP2GO: a comprehensive pan-species database on RNA-binding proteins, their interactions and functions. Nucleic Acids Res. *49*, D425–D436. https://doi.org/10.1093/nar/gkaa1040.
53. Stanietsky, N., Simic, H., Arapovic, J., Toporik, A., Levy, O., Novik, A., Levine, Z., Beiman, M., Dassa, L., Achdout, H., et al. (2009). The interaction of TIGIT with PVR and PVRL2 inhibits human NK cell cytotoxicity. Proc. Natl. Acad. Sci. USA *106*, 17858–17863. https://doi.org/10.1073/pnas.0903474106.
54. Fuchs, A., Cella, M., Giurisato, E., Shaw, A.S., and Colonna, M. (2004). Cutting Edge: CD96 (Tactile) Promotes NK Cell-Target Cell Adhesion by Interacting with the Poliovirus Receptor (CD155). J. Immunol. *172*, 3994–3998. https://doi.org/10.4049/jimmunol.172.7.3994.
55. Wojtowicz, W.M., Vielmetter, J., Fernandes, R.A., Siepe, D.H., Eastman, C.L., Chisholm, G.B., Cox, S., Klock, H., Anderson, P.W., Rue, S.M., et al. (2020). A Human IgSF Cell-Surface Interactome Reveals a Complex Network of Protein-Protein Interactions. Cell *182*, 1027–1043.e17. https://doi.org/10.1016/j.cell.2020.07.025.
56. Pende, D., Bottino, C., Castriconi, R., Cantoni, C., Marcenaro, S., Rivera, P., Spaggiari, G.M., Dondero, A., Carnemolla, B., Reymond, N., et al. (2005). PVR (CD155) and Nectin-2 (CD112) as ligands of the human DNAM-1 (CD226) activating receptor: involvement in tumor cell lysis. Mol. Immunol. *42*, 463–469. https://doi.org/10.1016/j.molimm.2004.07.028.
57. Abramson, J., Adler, J., Dunger, J., Evans, R., Green, T., Pritzel, A., Ronneberger, O., Willmore, L., Ballard, A.J., Bambrick, J., et al. (2024). Accurate structure prediction of biomolecular interactions with AlphaFold 3. Nature *630*, 493–500. https://doi.org/10.1038/s41586-024-07487-w.
58. Lucas, R., Gómez-Pinto, I., Aviñó, A., Reina, J.J., Eritja, R., González, C., and Morales, J.C. (2011). Highly Polar Carbohydrates Stack onto DNA Duplexes via CH/π Interactions. J. Am. Chem. Soc. *133*, 1909–1916. https://doi.org/10.1021/ja108962j.
59. Spitale, R.C., Flynn, R.A., Zhang, Q.C., Crisalli, P., Lee, B., Jung, J.-W., Kuchelmeister, H.Y., Batista, P.J., Torre, E.A., Kool, E.T., et al. (2015). Structural imprints in vivo decode RNA regulatory mechanisms. Nature *519*, 486–490. https://doi.org/10.1038/nature14263.
60. Castello, A., Fischer, B., Frese, C.K., Horos, R., Alleaume, A.-M., Foehr, S., Curk, T., Krijgsveld, J., and Hentze, M.W. (2016). Comprehensive Identification of RNA-Binding Domains in Human Cells. Mol. Cell *63*, 696–710. https://doi.org/10.1016/j.molcel.2016.06.029.
61. Cardin, A.D., and Weintraub, H.J. (1989). Molecular modeling of protein-glycosaminoglycan interactions. Arteriosclerosis *9*, 21–32. https://doi.org/10.1161/01.ATV.9.1.21.
62. Xue, S., Zhou, F., Zhao, T., Zhao, H., Wang, X., Chen, L., Li, J.-P., and Luo, S.-Z. (2022). Phase separation on cell surface facilitates bFGF signal transduction with heparan sulphate. Nat. Commun. *13*, 1112. https://doi.org/10.1038/s41467-022-28765-z.
63. Klein, K., Hölzemer, A., Wang, T., Kim, T.-E., Dugan, H.L., Jost, S., Altfeld, M., and Garcia-Beltran, W.F. (2021). A Genome-Wide CRISPR/Cas9-Based Screen Identifies Heparan Sulfate Proteoglycans as Ligands of Killer-Cell Immunoglobulin-Like Receptors. Front. Immunol. *12*, 798235. https://doi.org/10.3389/fimmu.2021.798235.
64. Xu, D., Young, J.H., Krahn, J.M., Song, D., Corbett, K.D., Chazin, W.J., Pedersen, L.C., and Esko, J.D. (2013). Stable RAGE-Heparan Sulfate Complexes Are Essential for Signal Transduction. ACS Chem. Biol. *8*, 1611–1620. https://doi.org/10.1021/cb4001553.
65. Sirois, C.M., Jin, T., Miller, A.L., Bertheloot, D., Nakamura, H., Horvath, G.L., Mian, A., Jiang, J., Schrum, J., Bossaller, L., et al. (2013). RAGE is a nucleic acid receptor that promotes inflammatory responses to DNA. J. Exp. Med. *210*, 2447–2463. https://doi.org/10.1084/jem.20120201.
66. Termaat, R.M., Brinkman, K., van Gompel, F., van den Heuvel, L.P.W.J., Veerkamp, J.H., Smeenk, R.J., and Berden, J.H. (1990). Cross-reactivity of monoclonal anti-DNA antibodies with heparan sulfate is mediated via bound DNA/histone complexes. J. Autoimmun. *3*, 531–545. https://doi.org/10.1016/S0896-8411(05)80019-8.
67. Park, H., Kim, M., Kim, H.-J., Lee, Y., Seo, Y., Pham, C.D., Lee, J., Byun, S.J., and Kwon, M.-H. (2017). Heparan sulfate proteoglycans (HSPGs) and chondroitin sulfate proteoglycans (CSPGs) function as endocytic receptors for an internalizing anti-nucleic acid antibody. Sci. Rep. *7*, 14373. https://doi.org/10.1038/s41598-017-14793-z.
68. Ren, Z., Li, R., Zhou, X., Chen, Y., Fang, Y., and Zou, P. (2023). Enzyme-Mediated Proximity Labeling Identifies Small RNAs in the Endoplasmic Reticulum Lumen. Biochemistry *62*, 1844–1848. https://doi.org/10.1021/acs.biochem.3c00142.
69. Zhang, M., Liu, L., Lin, X., Wang, Y., Li, Y., Guo, Q., Li, S., Sun, Y., Tao, X., Zhang, D., et al. (2020). A Translocation Pathway for Vesicle-Mediated Unconventional Protein Secretion. Cell *181*, 637–652.e15. https://doi.org/10.1016/j.cell.2020.03.031.
70. Luteijn, R.D., van Diemen, F., Blomen, V.A., Boer, I.G.J., Manikam, S.S., van Kuppevelt, T.H., Drexler, I., Brummelkamp, T.R., Lebbink, R.J., and Wiertz, E.J. (2019). A Genome-Wide Haploid Genetic Screen Identifies Heparan Sulfate-Associated Genes and the Macropinocytosis Modulator TMED10 as Factors Supporting Vaccinia Virus Infection. J. Virol. *93*, e02160-18. https://doi.org/10.1128/jvi.02160–02118.
71. Gruner, H.N., and McManus, M.T. (2021). Examining the evidence for extracellular RNA function in mammals. Nat. Rev. Genet. *22*, 448–458. https://doi.org/10.1038/s41576-021-00346-8.
72. Ma, M., Jiang, W., and Zhou, R. (2024). DAMPs and DAMP-sensing receptors in inflammation and diseases. Immunity *57*, 752–771. https://doi.org/10.1016/j.immuni.2024.03.002.
73. Nofi, C.P., Wang, P., and Aziz, M. (2022). Chromatin-Associated Molecular Patterns (CAMPs) in sepsis. Cell Death Dis. *13*, 700. https://doi.org/10.1038/s41419-022-05155-3.
74. Fischer, S., Gesierich, S., Griemert, B., Schänzer, A., Acker, T., Augustin, H.G., Olsson, A.-K., and Preissner, K.T. (2013). Extracellular RNA Liberates Tumor Necrosis Factor-α to Promote Tumor Cell Trafficking and Progression. Cancer Res. *73*, 5080–5089. https://doi.org/10.1158/0008-5472.CAN-12-4657.
75. Keith, M.P., Moratz, C., and Tsokos, G.C. (2007). Anti-RNP immunity: Implications for tissue injury and the pathogenesis of connective tissue disease. Autoimmun. Rev. *6*, 232–236. https://doi.org/10.1016/j.autrev.2006.08.007.

76. Faas, F.G.A., Avramut, M.C., van den Berg, B.M., Mommaas, A.M., Koster, A.J., and Ravelli, R.B.G. (2012). Virtual nanoscopy: Generation of ultra-large high resolution electron microscopy maps. J. Cell Biol. *198*, 457–469. https://doi.org/10.1083/jcb.201201140.

77. Rappsilber, J., Mann, M., and Ishihama, Y. (2007). Protocol for micro-purification, enrichment, pre-fractionation and storage of peptides for proteomics using StageTips. Nat. Protoc. *2*, 1896–1906. https://doi.org/10.1038/nprot.2007.261.

78. Tang, D., Chen, M., Huang, X., Zhang, G., Zeng, L., Zhang, G., Wu, S., and Wang, Y. (2023). SRplot: A free online platform for data visualization and graphing. PLoS One *18*, e0294236. https://doi.org/10.1371/journal.pone.0294236.

79. Spahn, P.N., Bath, T., Weiss, R.J., Kim, J., Esko, J.D., Lewis, N.E., and Harismendy, O. (2017). PinAPL-Py: A comprehensive web-application for the analysis of CRISPR/Cas9 screens. Sci. Rep. *7*, 15854. https://doi.org/10.1038/s41598-017-16193-9.

80. Martin, M. (2011). Cutadapt removes adapter sequences from high-throughput sequencing reads. EMBnet J. *17*, 10–12. https://doi.org/10.14806/ej.17.1.200.

81. Smith, T., Heger, A., and Sudbery, I. (2017). UMI-tools: modeling sequencing errors in Unique Molecular Identifiers to improve quantification accuracy. Genome Res. *27*, 491–499. https://doi.org/10.1101/gr.209601.116.

82. Bray, N.L., Pimentel, H., Melsted, P., and Pachter, L. (2016). Near-optimal probabilistic RNA-seq quantification. Nat. Biotechnol. *34*, 525–527. https://doi.org/10.1038/nbt.3519.

83. Perez-Riverol, Y., Bai, J., Bandla, C., García-Seisdedos, D., Hewapathirana, S., Kamatchinathan, S., Kundu, D.J., Prakash, A., Frericks-Zipper, A., Eisenacher, M., et al. (2022). The PRIDE database resources in 2022: a hub for mass spectrometry-based proteomics evidences. Nucleic Acids Res *50*, D543–D552. https://doi.org/10.1093/nar/gkab1038.

84. Joung, J., Konermann, S., Gootenberg, J.S., Abudayyeh, O.O., Platt, R.J., Brigham, M.D., Sanjana, N.E., and Zhang, F. (2017). Genome-scale CRISPR-Cas9 knockout and transcriptional activation screening. Nat. Protoc. *12*, 828–863. https://doi.org/10.1038/nprot.2017.016.

85. Evans, C., Hardin, J., and Stoebel, D.M. (2018). Selecting between-sample RNA-Seq normalization methods from the perspective of their assumptions. Brief. Bioinform. *19*, 776–792. https://doi.org/10.1093/bib/bbx008.

86. Love, M.I., Huber, W., and Anders, S. (2014). Moderated estimation of fold change and dispersion for RNA-seq data with DESeq2. Genome Biol. *15*, 550. https://doi.org/10.1186/s13059-014-0550-8.

87. Robinson, M.D., McCarthy, D.J., and Smyth, G.K. (2010). edgeR: a Bioconductor package for differential expression analysis of digital gene expression data. Bioinformatics *26*, 139–140. https://doi.org/10.1093/bioinformatics/btp616.

STAR★METHODS

KEY RESOURCES TABLE

REAGENT or RESOURCE	SOURCE	IDENTIFIER
Antibodies		
Goat Anti-Mouse IgM mu chain (Alexa Fluor® 488)	Abcam	ab150121; RRID:AB_2801490
Alexa Fluor® 488 AffiniPure Goat Anti-Human IgG (H+L)	Jackson Immunoresearch Laboratories	109-545-003; RRID:AB_2337831
Goat Anti-Mouse IgG H&L (Alexa Fluor® 488)	Abcam	ab150113; RRID:AB_2576208
Goat anti-Human IgG (H+L) Alexa Fluor 647	Thermo Fisher Scientific	A-21445; RRID:AB_2535862
anti-Heparan Sulfate IgM (clone F58-10E4)	AMSBio	370255-S; RRID:AB_3712773
TLR7 antibody (rabbit)	Novusbio	NBP2-24906; RRID:AB_2922764
HNRNPA1 Polyclonal antibody (rabbit)	Proteintech	11176-1-AP; RRID:AB_2117177
ENO1 Polyclonal antibody (rabbit)	Proteintech	11204-1-AP; RRID:AB_2099064
SSB Polyclonal antibody (rabbit)	Proteintech	11720-1-AP; RRID:AB_2877790
PA2G4 Polyclonal antibody (rabbit)	Proteintech	15348-1-AP; RRID:AB_2156602
Rabbit anti-DYKDDDDK tag	Proteintech	20543-1-AP; RRID:AB_11232216
Mouse anti-Heparan Sulfate 10E4 epitope (biotin-conjugated)	USBiological	H1890-01; RRID: AB_3719375
anti-FGF2 antibody (rabbit)	A gift from Geert-Jan Boons (UU/UGA)	N/A
Chemicals, peptides, and recombinant proteins		
1-step Ultra TMB-ELISA	Thermo Fisher Scientific	34028
2'-Azido-2'-dATP	Jena Bioscience	NU-976S
4% Paraformaldehyde (PFA)	Electron Microscopy Sciences	15710-S
AmpureXP beads	Beckman Coulter	A63880
Bovine Serum Albumin	Sigma Adrich	A7638
C18 Stagetips	3M Empore	Rappsilber et al.[77]
Chemiluminescent Nucleic Acid Detection Module Kit	Thermo Fisher Scientific	89880
cOmplete protease inhibitor	Roche	11836153001
DAPI	Roche	10236276001
DBCO-PEG_4-biotin	Sigma Adrich	760749
Dimethyl sulfoxide	Sigma Adrich	D8418
DMEM, high glucose, GlutaMAX™ Supplement, pyruvate	Gibco	31966047
DPBS 1x no calcium, no magnesium	Gibco	14190144
EDTA, 0.5 M, pH 8.0, Molecular Biology Grade	Sigma Adrich	324506
Eosin-5-isothiocyanate	Abcam	ab270343
ExoSAP-IT PCR Product Cleanup Reagent	Applied Biosystems	78201
FastAP	Thermo Fisher Scientific	EF0654
Fetal Bovine Serum	HyClone	SH30071.03HI
Glutaraldehyde, 25% aq. soln.	Thermo Fisher Scientific	A17876.0F
Ham's F-12K medium	Gibco	21127022
HBSS 1x	Gibco	14025092
Human CD96-Fc, carrier free	R&D systems	9360-CD
Human DNAM-1/CD226-Fc, carrier free	R&D systems	666-DN

(*Continued on next page*)

Continued

REAGENT or RESOURCE	SOURCE	IDENTIFIER
Human IgG isotype control	Invitrogen	02-7102
Human TIGIT-Fc, carrier free	R&D systems	9464-TG
Human TLR7-Fc, carrier free	R&D systems	9567-TR
Igepal CA-630	Sigma Adrich	I8896
Iodoacetamide	Sigma Aldrich	I1149
Isolate II Genomic DNA Kit	Meridian Bioscience	BIO-52065
KAPA HiFi HotStart ReadyMix	Roche	7958927001
KIR2DL5/CD158f -Fc, carrier free	R&D systems	6634-KR
LDS Sample Buffer (4X)	Invitrogen	NP0008
$MgCl_2$ 1M, RNase-free	Invitrogen	AM9530G
Dynabeads MyONE silane	Invitrogen	37002D
NaCl 5M, RNase-free	Invitrogen	AM9760G
NEBNext® Magnesium RNA Fragmentation Module	NEB	E6150S
NuPAGE™ Bis-Tris Mini Protein Gels, 4–12%	Thermo Fisher Scientific	NP0322BOX
Osmium Tetroxide	Electron Microscopy Sciences	19134
Panexin CD	Pan-Biotech	P04-93100
pCp-Biotin	Jena Bioscience	NU-1706-BIO
Penicillin-Streptomycin (10,000 U/mL)	Thermo Fisher Scientific	15140122
PMSF Protease Inhibitor	Thermo Fisher Scientific	36978
Polybrene Infection / Transfection Reagent	Millipore	TR1003G
Polyethyleneimine	Polyscience	24765
Protein A Dynabeads	Invitrogen	10001D
Protein A-HRP	Invitrogen	101023
Protein-A-gold 10nm	PAG10 nm/S	https://cellmicroscopy.nl/products/
PureLink RNase A	Invitrogen	12091021
Puromycin	Sigma Aldrich	P8833
RNase Cocktail Enzyme Mix	Invitrogen	AM2296
RNase I	Jena Biosciences	EN-176
RNaseIn	Promega	N2511
Sodium ascorbate	Sigma Adrich	A4034
Sodium azide	Sigma Adrich	S8032
Sodium Cacodylate Buffer, 0.2M	Electron Microscopy Sciences	11650
Sodium deoxycholate	Sigma Adrich	30970
Sodium dodecyl sulfate	Sigma Adrich	71725
Streptavidin	Invitrogen	434301
Streptavidin sepharose high-performance beads	Cytiva	15511301
SUPERaseIn™ RNase Inhibitor	Invitrogen	AM2696
SuperScript III reverse transcriptase	Invitrogen	18080093
T4 PNK	NEB	M0201
T4 RNA ligase high concentration	NEB	M0437M
Tris HCl pH 7 1M, RNase-free	Invitrogen	AM9850G
Tris HCl pH 8 1M, RNase-free	Invitrogen	AM9855G
TRIzol reagent	Invitrogen	15596026
Trolox	Sigma Adrich	391913
Trypsin, MS grade	Promega	V5280

(*Continued on next page*)

Continued

REAGENT or RESOURCE	SOURCE	IDENTIFIER
Turbo DNase	Invitrogen	AM2294
West Pico PLUS Chemiluminescent Substrate	Thermo Fisher Scientific	34580
Wheat Germ Agglutinin, Biotinylated	Vector Laboratories	B-1025-5
Yeast poly(A) polymerase	Jena Bioscience	RNT-006-S
Critical commercial assays		
Illumina sequencing (genetic screening study), NovaSeq6000	GenomeScan BV	https://genomescan.nl/
Illumina sequencing (SCOOPS hepRNA), NovaSeq X plus	BMKGENE GmbH	http://www.bmkgene.com/
Deposited data		
Genetic screening data in fastq format	European Nucleotide Archive	PRJEB88327
Proteomics data	PRIDE Partner Repository	PXD061693
SCOOPS RNA sequencing data	European Nucleotide Archive	PRJEB88260
Unprocessed images	Mendeley Data	doi: 10.17632/sjrv6wm5dh.1
Experimental models: Cell lines		
CHO-K1	ATCC	CCL-61
CHO pgsE-606	ATCC	CRI-2242
CHO pgsD-677	ATCC	CRI-2244
HEK293T	ATCC	CRL-3216
U2OS	A gift from Marvin Tanenbaum (Hubrecht Institute)	CVCL_0042
Mel526	A gift from Daniel Peeper (NKI)	CVCL_8051
HeLa	A gift from Sungchul Kim (PROSTECH)	CVCL_0030
Oligonucleotides		
See Table S7 for oligonucleotides used in this study.	N/A	N/A
Recombinant DNA		
CRISPR Brunello genome-wide knockout library	Addgene (A gift from David Root and John Doench)	73178
lentiCRISPR v2	Addgene (A gift from Feng Zhang)	52961
pTT3-SP-6xHis-KIR2DL5(FL)-FLAG	Addgene (A gift from Chris Garcia)	157623
pCMV-VSVG	Addgene (A gift from Bob Weinberg)	8454
pMDLg/pRRE	Addgene (A gift from Didier Trono)	12251
pRSV-REV	Addgene (A gift from Didier Trono)	12253
Software and algorithms		
ImageJ2 (2.3.0)	NIH	N/A
FlowJo (10.7.2)	FlowJo, LLC	N/A
Image Lab (6.1)	Bio-Rad	N/A
Proteome Discoverer (3.1)	Thermo Fisher Scientific	N/A
GraphPad Prism 10	Dotmatics	N/A
Matplotlib (3.7)	The Matplotlib development team	https://matplotlib.org/3.7.0/
Microsoft Excel for Microsoft 365 (version 2402)	Microsoft	N/A
SRplot	Tang et al.[78]	10.1371/journal.pone.0294236
BioRender	Science Suite Inc.	N/A
PinAPL-Py	Spahn et al.[79]	10.1038/s41598-017-16193-9
Cutadapt (4.9)	Martin[80]	10.14806/ej.17.1.200
UMI-tools (1.1.2)	Smith et al.[81]	10.1101/gr.209601.116

(*Continued on next page*)

Continued

REAGENT or RESOURCE	SOURCE	IDENTIFIER
Kallisto (0.51)	Bray et al.[82]	10.1038/nbt.3519
AlphaFold Server	Google DeepMind	https://alphafoldserver.com/
EndNote X7.8	Clarivate	N/A
Image Lab Touch Software (2.3.0.07)	Bio-Rad	N/A
Agilent 2100 Expert Software (B.02.12)	Agilent	N/A
BD FACSDiva	BD	N/A
CytExpert	Beckman Coulter	N/A
Xcalibur (4.7.69.73)	Thermo Fisher Scientific	https://docs.thermofisher.com/v/u/Xcalibur-4.7-Release-Notes
BioRender	BioRender	N/A
NIS Elements Confocal (6.10)	Nikon	N/A
Other		
μ-Slide 8 Well Glass Bottom chambers	ibidi	80827
Ultramicrotome	Leica, Vienna	UC6
Stratalinker UV crosslinker Model 1800	Stratagene	400072
Mini Gel Tank	Thermo Fisher Scientific	A25977
Protran Western blotting membranes	GE Life Sciences	GE10600094
0.45 μm low protein-binding membrane filter	Millipore	SLHP033RB
RNA Clean & Concentrator	Zymo Research	R1014
Clear Flat-Bottom MaxiSorp 96-Well Plates	Thermo Fisher Scientific	442404
MidiTrap G-25	GE Life Sciences	28922530
Cytoflex LX	Beckman Coulter	C11186
FACS Canto II	BD	338960
Nikon confocal A1R / SIM Scanning confocal	Nikon	https://www.tudelft.nl/tnw/over-faculteit/afdelingen/bionanoscience/research/facilities/kavli-nanolab-imaging-centre/microscope-acquisition/nikon-confocal-a1r-sim-scanning-confocal
Nanoflow HPLC system, Easy-nLC 1000	Thermo Fisher Scientific	LC120
Mass spectrometer Orbitrap-Exploris 480	Thermo Fisher Scientific	BRE725539

EXPERIMENTAL MODEL AND STUDY PARTICIPANT DETAILS

Cell culture

Mel526, U2OS and HeLa cells were cultured in DMEM (Thermo Fisher Scientific, 31966047) supplemented with 10% Fetal Bovine Serum (FBS, HyClone, SH30071.03HI) and 1x Penicillin-Streptomycin-Glutamine (Thermo Fisher Scientific, 10378016, 100x) at 37°C with 5 % CO_2. Wild-type Chinese Hamster Ovarian (CHO) (CHO-K1, ATCC, CCL-61) and heparan sulfate deficient mutant cell lines - CHO pgsE-606 and pgsD-677 (ATCC, CRI-2242 and -2244, respectively) were cultured in Ham's F-12K medium (Thermo Fisher Scientific, 21127022) supplemented with 10% FBS and 1x Penicillin-Streptomycin and Glutamine at 37°C with 5 % CO_2. To minimize possible influence from components in bovine serum, Mel526 cells and the mutant cells were also adapted into 1x Penicillin-Streptomycin-Glutamine-supplemented DMEM containing 1% FBS and 9% chemically defined serum replacement (Panexin CD, Pan-Biotech, P04-93100), following the protocol suggested by the supplier. Prior to experiments, cell culture flasks or dishes were replenished with DMEM containing 10% Panexin-CD without FBS.

METHOD DETAILS

Immunocytochemistry

Cells were fixed 24 hours post-seeding in μ-Slide 8 Well Glass Bottom ibidi chambers (ibidi, 80827, ~30,000 cells/well) with 4% Paraformaldehyde (PFA) aqueous solution (Electron Microscopy Sciences, 15710-S) in PBS for 10 min at RT and washed with PBS twice. Blocking was performed with blocking buffer containing 3% Bovine Serum Albumin in PBS (Sigma, A7638) for 1 hour at RT in RNase-free conditions by adding SUPERaseIn™ RNase Inhibitor (Thermo Fisher Scientific, AM2696, 1:200). For RNA competition, a synthetic

RNA oligo (Dharmacon™) with a sequence 5'-pGUCUUCAAAACUAGGUCGUUUUAGA-3'/biotin/ was added at 10 μM during TLR7-Fc incubation. For RNase-treated samples, RNase Cocktail Enzyme Mix (Thermo Fisher Scientific, AM2296, 1:100) was added to the blocking buffer. Post-blocking, recombinant proteins or primary antibodies were added to cells prepared in the same respective blocking buffer and incubated at 21°C for 1 hour. Cells were washed 3 times with PBS (2 minutes per wash) followed by the addition of secondary antibodies prepared in the blocking buffer along with DAPI (Roche, 10236276001, 1 μg/mL final concentration) and incubated at 21°C for 1h. The cells were washed with PBS and imaged with confocal microscopy (Olympus A1R SiM, oil immersion, filter settings for Red (Alexa-546 and others: excitation 551nm, emission 565 nm); Blue (DAPI: excitation 358 nm, emission 463 nm); Green (Alexa-488 and others: excitation 490nm, emission 544nm) and Far-red (Alexa-647 and others: excitation 650 nm, emission 671 nm).

Electron microscopy

U-2 OS cells were cultured in a 6 cm petri dish at 90-100% confluency. To avoid fixation-induced artefacts, live cells were first stained for csRNA by incubating on ice for 30minutes and then applying TLR7-Fc (3% Bovine Serum Albumin in PBS, final conc 2.5 μg/mL) for 1 hour on ice followed by thorough washing and incubation with PAG-10 (Protein-A-gold 10nm, PAG10 nm/S, OD50,Cell Microscopy Core, UMC Utrecht) solution in PBS (1:50) on ice for 30minutes. Immunogold-labelled cell monolayers were fixed in 1.5% glutaraldehyde in 0.1 M sodium cacodylate buffer for 2 hours before being successively incubated in 1% osmium tetroxide in 0.1 M cacodylate buffer for 1 hour and in 1% uranyl acetate in water for 1 hour. The cells were then dehydrated through a series of incubations in ethanol (70-100%) for 90 minutes and embedded in Epon. The flat embedded cells were sectioned with an ultramicrotome (UC6, Leica, Vienna) using a 35 degrees diamond knife (Diatome, Biel, Switzerland) at a nominal section thickness of 70 nm. The sections were transferred to a formvar and carbon coated 200 mesh copper grid and stained for 20 minutes with 7% uranyl acetate in water and for 10 minutes with lead citrate. EM images were recorded using a Tecnai 12 electron microscope (Thermo Fisher Scientific) equipped with an EAGLE 4k×4k digital camera. For navigation on EM images, montages of images at 11,000× were generated using stitching software. The stitched images were imaged and annotated using Aperio ImageScope (Leica Biosystems).

Flow cytometry analysis of csRNA on live cells

Cells cultured to 80-90% confluency were washed once with 1x DPBS after removing culture media, and then lifted with 10 mM EDTA (diluted from 0.5M sterile filtered stock solution) in 1x DBPS at 37 °C for 5 minutes. Lifted cells were dispensed into a 96-well FACS plate with 2-2.5 x10^5 cells per well. For extracellular RNase treatment, PureLink RNase A (Thermo Fisher Scientific, 12091021) were added to the lifting buffer at a final concentration of 40 μg/mL. After spinning down at 300 g for 5 minutes at 4°C and supernatant removal, cells in each well were resuspended in 30 μL of TLR7-Fc or other Fc-tagged proteins (final concentration 5 μg/mL) in 0.5% BSA in 1x DPBS containing 200U/mL RNasein (Promega, N2511), and incubated on ice for 45 minutes. For secondary only control, cells were incubated with 30 μL 0.5% BSA in 1x DPBS. After incubation, 200 μL cold 1x DBPS were added to each well and the plate was spun down at 300 g for 5 minutes at 4°C. After supernatant removal, cells were resuspended in 30 μL of goat-anti-human IgG AlexaFluor647 conjugate (Thermo Fisher Scientific, A-21445) in 0.5% BSA in 1x DPBS, and incubated in dark for 30 minutes on ice. Upon completion, 200 μL cold 1x DBPS were added to each well and the plate was spun down at 300 g for 5 minutes at 4°C. Finally, cells were resuspended in 200 μL cold 0.5% BSA in 1x DPBS containing 0.1 μg/mL DAPI. The cells were then analyzed on a flow cytometer using HTS settings. Typically, 150 μL cell suspension per well was infused in the system for analysis, with a flow rate of 1 mL/minute.

TLR7-Fc binding rescue by exogenous RNA

Cells were processed as was described above, except for that after detachment with EDTA buffer containing Purelink RNase A, cells were spun down, resuspended in 1x DPBS containing 200 U/mL RNasein, with varying concentration of total cellular RNA (2 – 0.2 mg/mL), incubated at 4 °C for 30 minutes, and washed with cold 1x DPBS, before incubating with TLR7-Fc. The rest of the steps followed exactly the above flow cytometry experiment.

TLR7-RNA crosslinking, precipitation, and on-bead RNA labelling

The procedure after TLR7-Fc binding follows that of eCLIP with modifications.[29] Cells in a 15 cm dish at 90% confluency were washed once with 1x DPBS following culture media removal, and was then incubated with 3 mL per dish 10 mM EDTA in 1x DPBS at 37°C for 5 minutes. Another 7 mL 1x DPBS was added to the dish to wash cells off the dish. The total of 10 mL cell suspension was transferred to a 15 mL Falcon tube. The dish was washed further with 5 mL 1x DPBS, which was then combined in the same tube. The cells were spun down at 300 g for 5 minutes at 4°C, and the supernatant was removed. The cell pellets were taken up in 250 μL TLR7-Fc (final concentration 5 μg/mL) in 0.5% BSA in 1x DPBS containing 200U/mL RNasein, and the suspension was put on ice for 30 minutes, with gentle tapping every 10 minutes. The tube was topped up to 15 mL with cold 1x DPBS, and spun down at 300 g for 5 minutes at 4°C. The pellets were washed twice with 10 mL cold 1x DPBS. The cells in the second wash were directly transferred to a 10 cm dish for UVC crosslinking on ice without the lid using Stratalinker (400 mJ setting). After UVC exposure, cells were transferred back to the tube and spun down. For TLR7 non-crosslinked control, cells after lifting were transferred into a 15 mL Falcon tube and spun down, resuspended in 10 mL 1x DPBS, and transferred to a 10 cm dish for crosslinking. After crosslinking, cells

were transferred back to the 15 mL tube and spun down, and incubated with the TLR7-Fc solution, which was followed by two washes.

The pellets from above were lysed in 400 μL lysis buffer (50 mM Tris-HCl pH 7.4, 100 mM NaCl, 1% v/v Igepal CA-630, 0.1% v/v SDS, 0.5% w/v sodium deoxycholate) containing 1x cOmplete protease inhibitor (Roche, 11836153001) cocktail and 1mM PMSF. The solution was sonicated at 20% power for 5 minutes (10s on, 10s off) on ice. To the sonicated lysate was added 2 μL TurboDNase (Thermo Fisher Scientific, AM2238), and 4 μL diluted RNase I (Thermo Fisher Scientific, AM2294, prediluted 1:20 in 1x DPBS). The lysate was then incubated at 37°C for 5 minutes, followed by the addition of 4 μL SUPERaseIn. To prepare magnetic beads for TLR-Fc precipitation, 10 μL per dish protein A Dynabeads (Thermo Fisher Scientific, 10001D) was washed twice with lysis buffer before added to the above RNA-fragmented lysate. The bead suspension was incubated on an end-to-end rotator at 4 °C for 2 hours. The beads were then wash twice with 200 μL CLIP high salt buffer (50 mM Tris-HCl pH 7.4, 1 M NaCl, 1% Igepal CA-630, 1 mM EDTA, 0.1% SDS, 0.5% sodium deoxycholate), three times with 200 μL CLIP low salt buffer (20 mM Tris-HCl pH 7.4, 10 mM $MgCl_2$, 0.2% Tween-20, 5 mM NaCl). The precipitated RNA-TLR7-Fc was 3'-end repaired on-bead by incubating with FastAP (Thermo Fisher Scientific, EF0654, 1 U), T4 PNK (NEB, M0201, 20 U), TurboDNase (0.4 U) and SUPERaseIn (5 U) in 10 μL 1x PNK buffer without DTT at 37 °C for 30 minutes, followed by the same wash procedure. The end-repaired RNA was subjected to on-bead 3'-end biotinylation by incubating with 20 nM pCp-biotin, T4 RNA ligase high-concentration (NEB, M0437M, 30 U) and SUPERaseIn (5 U) in 1x RNA ligase buffer without DTT, containing 1 mM ATP, 3.6% DMSO, 0.025% Tween-20 and 18% w/v PEG-8000 16 °C overnight, which was followed the same wash procedure. After the final wash, beads were directly taken up in 1x LDS sample loading buffer containing 1x sample reducing solution, denatured at 75 °C for 10 minutes. The samples were resolved on an NuPAGE™ 4 -12% bis-Tris mini protein gel, wet transferred onto a nitrocellulose (NC) membrane at 30 V for 4 hours at 4 °C, and subjected to chemiluminescent biotinylated nucleic acid detection. The same NC membrane was finally subjected to Western blot for TLR7 detection using rabbit anti-human TLR7 (1:1000) in combination with horse radish peroxidase (HRP)-conjugated goat-anti-ribbit secondary antibody (1:5000).

Proximity biotinylation of csRNA-proximal proteome

The experiment was performed using three independent cell cultures for each treatment. Cells in a 15 cm dish at 90% confluency were washed twice with 1x DPBS after removing culture media, and was lifted with 3 mL per dish 10 mM EDTA in 1x DPBS. For csRNA-digested sample, RNase A was added to the lifting buffer at a final concentration of 40 μg/mL. 1x DPBS was used to bring cell suspension to 10 mL, which was transferred to a 15 mL Falcon tube. The dish was washed with 5 mL 1x DPBS, which was combined in the same tube. The cells were spun down at 300 g for 5 minutes at 4°C, and pellets were incubated for 30 minutes at 4 °C with per dish 250 μL solution of precomplexed TLR7-Fc (5 μg/mL final concentration) and protein-A-HRP conjugate (Thermo Fisher Scientific, 101023, 7 μg/mL final concentration) in 0.5% BSA in 1x DPBS containing 200U/mL RNasein. For an IgG isotype control, human IgG (Thermo Fisher Scientific, 02-7102) was premixed with protein-A-HRP at the same concentration. Cells were washed three times with cold 1x DPBS, and spun down at 200 g for 2 minutes at 4 °C each time. After the final wash, the pellets were resuspended in 1 mL per sample 500 μM biotin-phenol in 1x DPBS, and let sit for 1 minute at room temperature. 1 mL 2 mM hydrogen peroxide in 1x DPBS was added to each sample and mixed well. This mixture was incubated for 2 minutes at room temperature and 10 mL cold quenching buffer (5 mM Trolox + 10 mM sodium ascorbate + 10 mM sodium azide in 1x DPBS) was directly added to the sample. The cells were washed two more times with quenching buffer, and were lysed in 300 μL per sample RIPA buffer (50 Mm Tris pH 7.5, 150 mM NaCl, 0.5% sodium deoxycholate, 0.1% SDS, 1% NP40) containing 1x cOmplete™ protease inhibitor cocktail and 1mM PMSF. The lysate was sonicated to clarity, and was spun down at 21,000 g for 10 minutes at 4°C. An aliquot of the supernatant was taken for WB to detect biotin signal, and the rest was subjected to enrichment of biotinylated proteins.

The pellets were taken up in RIPA buffer. The supernatant from the sonicated lysates was subjected to bead enrichment with 12.5 μL per sample streptavidin sepharose high-performance beads (Cytiva, 15511301) on an end-to-end rotator for 2 h at room temperature. The beads were washed 5 times with 500 μL RIPA buffer and 4 times with 500 μL PBS, prior to LC-MS/MS sample preparation.

Proteomics sample preparation and LC-MS/MS analysis

Beads from biotin affinity pulldown were incubated with 50 μL elution buffer (2 M Urea, 10 mM DTT, 100 mM Tris pH 8) on a thermoshaker at 1250 rpm for 20 minutes at room temperature. Iodoacetamide (50 mM final concentration) was then added, and the samples were incubated in a thermoshaker at 1250 rpm in dark for 10 minutes at room temperature. 2.5 μL of trypsin (0.1 mg/mL stock solution) was then added, followed by incubation in a thermoshaker at 1250 rpm for 2 hours at room temperature. Samples were spun down (1500 x *g*, 2 min, RT) and supernatant was collected. Another 50 μL elution buffer was then added to the beads, which were incubated on a thermoshaker at 1250 rpm for 5 minutes at room temperature. Beads were then spun down (1500 x *g*, 2 min, RT), and the supernatant collected and combined with the first elution. 1 μL trypsin (0.1 mg/mL) was added and the samples were incubated overnight at room temperature. Tryptic peptides were acidified by adding 10 μL 10% (v/v) TFA, and purified using C18 Stagetips[77] (3M Empore). Briefly, StageTips were prepared and washed with methanol followed by a wash with buffer B (80% acetonitrile and 0.1% formic acid) and two washes with buffer A (0.1% formic acid). All washes were done at 1500 × *g* for 4 min at RT. Samples were loaded onto the StageTips and centrifuged at 600 × *g* for 10 min at RT and washed once with buffer A. StageTips were stored at 4°C

Peptides were eluted from StageTips with 30 ml of buffer B, reduced to a volume of 5 ml by Speedvac centrifugation, after which 7 ml of buffer A (0.1% formic acid) was added. For the TLF7 proximity labeling experiments, 6 µl of each sample was loaded on an Easy LC1000 (Thermo Scientific) connected to an Orbitrap Exploris 480 (Thermo Scientific). The machine was operated in data-dependent acquisition (DDA) mode, with acquisition time set at 60 minutes. An acetonitrile gradient of 12-30% in 43 minutes was used followed by an increase of the acetonitrile concentration to 60% in 10 minutes and to 95% in 1 minute. The full scan of the peptides was set to a resolution of 120,000 in a scan range of 350–1300m/z.

Proteomics data analysis

Raw mass spectrometry data were analysed using Proteome Discoverer version 3.1 (Thermo Scientific) and searched against the human UniProt/SwissProt database.

For DDA, we used the built-in processing workflow ''PWF_OT_Precursor_Quan_and_LFQ_CID_SequestHT_Percolator'' and the built-in consensus workflow ''CWF_Comprehensive_Enhanced Annotation_LFQ_and_Precursor_Quan'', with default settings. For the Sequest HT search, database parameters were enzymatic digestion with trypsin allowing two missed cleavages, a minimum peptide length of 6 amino acids and a maximum peptide length of 144 amino acids. We used a precursor mass tolerance of 10 ppm and a fragment mass tolerance of 0.6 Da. Cysteine carbamidomethylation was included as a static modification (57.021 Da), while methionine oxidation (15.995 Da) and protein N-terminal acetylation (42.011 Da) were included as dynamic modifications. FDR filtering was performed via percolator with a strict target FDR of 0.01 and a relaxed FDR of 0.05. Strict parsimony was applied for protein grouping, and unique plus razor peptides were used for quantification. Peptide quantification normalization was applied based on total peptide amount. Imputation Mode was set to ''Low Abundance Resampling''. ''Proteins'' tab was exported for downstream processing and statistical analysis with R.

For downstream processing, proteins were first filtered for having at least 2 unique peptides. Proteins containing "KRT" in their names as well as proteins with less than 3 values in at least 1 condition were filtered out. Statistical analysis was done using the DEP package, which uses a Student's t-test. Criteria for enrichment are listed in the figure legends. Volcano plots were generated by plotting the –log10 of the p-value against the log2 fold change. Gene ontology term searches for identified hits were performed using RBP2GO.

The proteomics datasets have been deposited in the ProteomeXchange Consortium via the PRIDE[83] partner repository with the dataset identifiers PXD061693.

Genetic screening and data analysis

For knockout screening, the human CRISPR Brunello genome-wide knockout library was a gift from David Root and John Doench (Addgene 73178). For virus production, HEK 293T cells were transfected with packaging plasmids pRSVrev, pHCMV-G VSV-G and pMDLg/pRRE together with the Brunello plasmid using polyethyleneimine (Polyscience Inc.). Virus was harvested, filtered and 150 million Mel526 melanoma cells (a kind gift from Daniel Peeper) were transduced in the presence of 8 µg/ml polybrene (Millipore) at an MOI of 0.3. Transduced cells were selected using puromycin (1 µg/ml) and after seven days, two batches of cells were stained for surface RNA using TLR7-Fc and the lowest 5% of expressing cells were sorted. Cells were grown out and sorted again using the same gating strategy as for the first sort. After this sort, genomic DNA was isolated using an Isolate II genomic DNA kit (GC Biotech) following supplier's manual for both the unsorted and sorted populations. gDNA was amplified using the primers for both the unsorted and sorted populations using the established protocol.[84] gRNAs were sequenced using the Illumina NovaSeq6000 and inserts were mapped to the reference. Analysis of gRNA enrichment was done using PinAPL-Py.[79]

Genetic screening hit validation

Hits from the knockout screen were validated using the top scoring gRNAs of each gene, which were cloned into the lentiCRISPR v2 vector (a gift from Feng Zhang, Addgene plasmid no. 52961). Mel526 cells were stably transduced with these gRNAs, selected using puromycin, and pooled knockout cells were used for the analysis. Guide sequences were as follows: EXT2, 5′-CACCGTGGTTAAG CACATCGATGGA-3′; EXTL3, 5′-CACCGAAATGAACCTCGGTAACACG-3′; HS6ST1, 5'-AAACCCGCGAGACTTGGCTCTTCTC-3', C3orf58, 5'-CACCGGCAGACGCACGTCGCCGTTG-3'. Mutant cells were subjected to flow cytometry analysis to check for TLR7-Fc binding, following the procedure described above.

Preparation of PVR KO mutant cells

HEK293T cells (ATCC, CRL-3216) were seeded into 10 cm dishes at 60–70% confluency for lentiviral packaging. The guide RNA sequence used was 5'-ATTGGTGCCCTCAAGCCAGG-3' (PVR, NM_006505.4, NC_000019.10, sense, exon position: 44650019). For each 10 cm dish, 5.63 µg pCMV-VSVG (Addgene #8454), 8.55 µg pMDLg/pRRE (Gag/Pol) (Addgene #12251), 4.5 µg pRSV-REV (Addgene #12253), and 11 µg lentiCRISPR v2 lentiviral transfer plasmid containing the sgRNA (Addgene #52961) were diluted in serum-free DMEM (Gibco, 41965-039) to a total volume of 500 µL. In a separate tube, 90 µg of polyethylenimine (PEI, linear 25 kDa, Polysciences, #23966) was mixed with serum-free DMEM to a final volume of 500 µL. The PEI mixture was then added dropwise to the DNA mixture, gently mixed, and incubated for 15–30 min at room temperature. The resulting transfection complex was added dropwise to the cells together with 4 mL serum-free DMEM. After 4 h, 4 mL DMEM containing 20% fetal bovine serum (FBS; Gibco, 10270-106) was added. Cells were incubated overnight at 37°C in 5% CO_2. Forty-eight hours post-transfection, viral supernatant was collected, centrifuged at 3000 rpm for 10 min at 4°C, and filtered through a 0.45 µm low protein-binding membrane filter (Millipore,

SLHP033RB). Viruses were either used immediately or stored at −80°C. For transduction, target HEK293T cells were cultured in DMEM (Gibco, 41965-039) supplemented with 10% FBS and 1% penicillin-streptomycin (Gibco, 15140-122). Cells were transduced using 30% viral supernatant and 5 μg/mL Polybrene (Sigma-Aldrich, TR-1003-G). Forty-eight hours later, transduced cells were selected with 3 μg/mL puromycin (Sigma-Aldrich, P8833).

UVC and eosin Y-mediated crosslinking and orthogonal organic phase separation (OOPS)

For suspension cells such as K562 (used in this study), start with ~20 million. Culture media was removed and the cells were wash twice with 10 ml DPBS. Cell pellets were resuspended in 10 ml DPBS, and transferred into a 10 cm dish. For UVC crosslinking, the cells (without lid) were then UV-crosslinked with a Stratalinker 1800 chamber at 254 nm for 5 min on ice. The crosslinked pellets were collected and directly lysed in 1 ml TRIzol per million cells. For EY-mediated crosslinking, cells after wash were resuspended in DPBS containing 50 μM eosin Y (CAS #17372-87-1). The cells were placed in dark at room temperature for 2 min and put on ice with lid open. The cells were exposed to green light (100 W chip-on-board) for 10 min. The crosslinked pellets were collected and directly lysed in 1 ml TRIzol per million cells.

For adherent cells, start at least with a 10 cm dish. Culture media was removed and the cells were wash twice with 10 ml HBSS. In case of UVC crosslinking, upon removal of the wash solution, the dish without the lid was placed in the chamber on ice, and exposed to UV for 5 min. The crosslinked cells were lysed in 1 ml TRIzol per 10 cm dish, and scraped to one side of the dish and transferred to a 2 ml Eppendorf tube. In case of EY-mediated crosslinking, 7 ml HBSS containing 50 μM eosin Y was added to the dish. The dish without lid was exposed to green light for 10min and washed once more with HBSS, followed by cell lysis in 1 ml TRIzol per 10 cm dish, scraping and the transfer as mentioned ealier.

When performing AGPC extraction of total RNA (from the blue 1st aqueous phase in Figure S4A, without repeated OOPS), we observed substantial thickening of the interphase, and a dropped yield of RNA isolated from the aqueous phase (Figure S4B). We reasoned the RNA must have been brought to the interphase (off-white phase in Figure S4A), a similar effect which occurs when the cells are exposed to UVC irradiation.[46] UVC irradiation creates covalent bonds between the RNA and the bound proteins, making the complexes into an amphiphilic entity. This physical nature of crosslinked RNA-protein complexes retains them in the AGPC interphase.

OOPS was performed following reported literature. Unless otherwise noted, the phase separation procedure and the amounts of enzymes and duration of incubation for releasing RNA-bound proteins and protein-bound RNA remain the same as reported. In brief, 0.2 ml chloroform per 1 ml TRIzol was added to the tube, followed by vortexing and spin-down at 4°C. The aqueous and organic phases were carefully removed with a blunt needle without touching the interphase. Such procedure was repeated 3 times for UVC crosslinking and 4 times for EY crosslinking. The cleaned interphase was then precipitated with methanol. The resulted pellets were wash once again with methanol and air-dried for 5 min.

To isolate protein-bound RNA, the interphase pellet was directly treated with proteinase K solution. The protein-degraded RNA samples were then purified with TRIzol in combination of Zymo RNA Clean & Concentrator columns (Zymo Research C1008) following the product manual. The yield of RNA isolated from the first aqueous phase was calculated by measuring the concentration with nanodrop. The cleaned RNA samples were then subjected to 1% agarose gel electrophoresis and stained with SybrGold (Figure S4C). Same volume of RNA solution across all samples were loaded in the gels. The stained gel was imaged with a ChemiDoc system using SybrGold settings.

To isolate RNA-bound proteins, the interphase pellet was redissolved in 1% SDS containing ammonium bicarbonate. The RNA was fragmented by sonication and Mg(II) ions at 94°C. To the resulted solution,The digestion was incubated at 37°C for 20 hours, followed by another round of TRIzol phase separation. RNase Cocktail was added. RNA degradation removes the amphiphilic property of the RNA-bound proteins. The RNA-bound proteins should be released into the pink organic phase as shown in Figure S4D. These proteins were collected from the pink organic phase and precipitated with methanol, redissolved in 1% SDS. An equal volume of each sample solution was taken for SDS-PAGE and Western blot. To check for total isolated proteins, the gel was Coomassie-stained and scanned under a ChemiDoc system (Figure S4E). Same volume of protein solutions were loaded across all samples. We also used Western blot to detect known RBPs, including heterogeneous nuclear ribonucleoprotein A1 (HNRNPA1), enolase 1 (ENO1), Sjögren syndrome antigen B (SSB) (Figure S4F). The PVDF membrane post-transfer was blocked with 5% BSA in TBST (blocking buffer), incubated with the corresponding primary antibody (1:1000 dilution for all) in blocking buffer, washed 3 times with TBST, and incubated with the secondary antibody (1:5000 – 1:10000) in blocking buffer. The resulted membrane was washed 3 times, treated with West Pico PLUS Chemiluminescent Substrate (Thermo Fisher Scientific, 34580), and imaged under a ChemiDoc system.

Conjugation of eosin isothiocyanate to streptavidin

Eosin 5-isothiocyanate (Abcam, ab270343) was dissolved in DMSO to make a 100mM stock solution. The conjugation reaction was performed for 500 μg streptavidin in 0.5 ml 1X DPBS at pH 8, with eosin isothiocyanate at a final concentration of 2mM. The reaction was allowed to proceed for 2 hours at room temperature, with shaking and in dark. The resulting mixture was purified twice with MidiTrap G-25 (GE Life Sciences, 28922530) columns, and buffer exchanged into 1x DPBS pH 7.4. The purified conjugate was stored at 4 °C in dark.

Enzyme-linked immunosorbent assay (ELISA) of EY-conjugated streptavidin

The 96-well MaxiSorp microtiter plate was coated with either streptavidin-EY or unmodified streptavidin at 10 μg/ml in 100mM $NaHCO_3$ overnight in dark at room temperature. The wells were washed twice with PBS and then blocked with 2% BSA in PBST

(blocking buffer) 1 hour in dark at room temperature. Serial dilutions (3x, starting concentration 10 μg/ml) of a biotinylated mouse monoclonal antibody (BioLegend, 317320) in blocking buffer were added to each row, and was incubated for 1 hour in dark at room temperature, followed by washing 3 times with PBST. To each well, HRP conjugated alpaca-anti-mouse (Jackson ImmunoResearch, 615-035-214) in blocking buffer was added and allowed to incubate for 45 minutes in dark at room temperature, followed by washing 3 times with PBST. Finally, 1-step Ultra TMB-ELISA (Thermo Fisher Scientific, YJ4085531) and incubated for 2 mins, and was stopped by 2M sulfuric acid. The optical density at 450 nm (OD450) was measured by a microtiter plate reader.

Spatio-selective crosslinking followed by OOPS (SCOOPS)

Cells at 85-90% of confluency in a 10 cm dish was used for each sample. For csRNA degradation, cells were treated with 13 μl of RNase A (Thermo Fisher Scientific, 12091021) and 3.2 μl of RNase I (Jena Biosciences) in 6.5 mL culture media under standard culturing condition (37℃, 5% CO_2 and humidified atmosphere) for 30 mins. All cells were washed with HBSS, and were incubated with 6 ml culture media containing 5 μg/ml biotinylated WGA (Vector Laboratories, B-1025) at 4°C for 1 hour. The corresponding negative control was with merely 6 ml culture media without biotinylated WGA. After aspiration, cells were washed twice with HBSS and then incubated with 6ml of culture media containing 2.5 μg/ml streptavidin-EY at 4°C for 30 mins in dark, after which the cells were washed twice with HBSS. The corresponding negative controls was with unmodified streptavidin in the culture media. 6mL HBSS was added to each plate prior to green light irradiation at 4°C for 10 mins. Supernatant was immediately removed after irradiation and the cells were lysed in 1.4ml TRIzol per dish, scraped and transferred into a 2 ml Eppendorf tube for OOPS. The OOPS procedure is the same as described earlier. Protein-bound RNA was released from interphase, purified, and subjected 3'-end Cy5 ligation, which followed the same procedure for 3'-end biotin ligation described above, except for the purification was performed using Zymo RCC-5 columns. 2% (v/v) of the first aqueous phase containing total cellular RNA was taken as loading control, and was also ligated with Cy5.

RNA sequencing library preparation

The RNA sequencing library preparation procedures are adapted from what was described for 'size-matched input' in the published reports.[29] RNA samples were first quality checked by Bioanalyzer. It is important to note not all interphase RNA is hepRNA. The electropherograms of SCOOPS_KO samples and the agarose gel results (Figures 4G and 4H) indicate the SCOOPS interphase contains more RNA components than exclusively hepRNA, as shown by the two prevalent peaks observed in the bioanalyzer traces of SCOOPS_KO samples include one in small RNA region (fewer than 200 nucleotides), and the other aligned well with 28S ribosomal RNA (rRNA) (Figure S5A). The peaks may be given rise to by RNA species exhibiting an intrinsic physical property to be retained in the interphase regardless of whether SO-crosslinked. The SCOOPS interphase could also contain originally intracellular RNA from, for instance, cell debris, which could be randomly crosslinked by singlet oxygen generated at the cell surface. In addition, the interphase may also contain cell-surface localized RNA species whose presentation is not dependent on HS, which is out of the scope of this study. Importantly, SCOOPS_KO samples can provide indications for hepRNA-irrelevant RNA species intrinsically associated with the SCOOPS procedure. These RNA species can serve as background in RNA sequencing data analysis.

All library preparations started with 150 ng (Qubit RNA quantification, broad range) RNA input. In brief, the RNA was first subjected to 3'-end repair (total volume 20 μl per sample): 2 μl 10x T4 PNK buffer, 2 μl FastAP, 1 μl T4 PNK, 0.5 μl SuperRasIn, 0.5 μl Turbo DNase, 37 °C, 45 min, 900 rpm on a thermoshaker. The end-repaired RNA was purified using TRIzol in combination with Zymo RCC-5 columns following the product manual, and eluted in 10 μl nuclease-free water. The pre-adenylated 3'-adapter was ligated using the following procedure (total volume 20 μl per sample): 2 μl 10x RNA ligase buffer, 10 μM (final concentration) pre-adenylated adapter, 6 μl 50% PEG8000, 0.3 μl DMSO, 0.5 μl SuperRasIn, 2 μl T4 RNA ligase 1 high concentration, 16 °C, 3h, 1000 rpm on a thermoshaker. The excess adapter was degraded post-ligation using 1 μl 5′ deadenylase (NEB, M0331S) and 2 μl RecJf (NEB, M0264S) after adding 2.5 μl 10x NEB buffer 1. The mixture was purified using TRIzol in combination with Zymo RCC-5 columns, and eluted with 10 μl nuclease-free water. Reverse transcription was performed with the following protocol: 4 μl 5x first strand buffer, 10 mM DTT, 0.8 mM dNTP, 0.5 μl SuperRaseIn, 1 μl SuperScript III (Thermo Fisher Scientific, 18080093), 55 °C, 30 min, on PCR heat block. The excess primer was degraded using 3 μl ExoSAP-IT, quenched with 1 μl 0.5 M EDTA. RNA was then removed under alkaline pH (3 μl 1 M NaOH) at elevated temperature (70 °C, 12 min) and neutralized with 3 μl 1 M HCl. The resulted complementary DNA (cDNA) was purified using MyOne Silane beads, and eluted with 20 μl nuclease-free water. Half of the purified cDNA was subjected to PCR amplification with NEBNext Multiplex Oligos for Illumina: 30 μl total reaction volume, 2x KAPA HiFi HotStart ReadyMix (Roche, 07958927001), 0.3 μM forward and reverse primers. Initial denaturation, 95 °C, 3 min; denaturation, 98 °C, 20 s; annealing, 65 °C, 15 s; extension, 72 °C, 15 s; total cycle number, 16; final extension, 72 °C, 1 min. The amplified library was first purified with AmpureXP beads (Beckman Coulter, A63880) and then size-selected using PAGE gel electrophoresis. The resulted libraries were quantified on a Qubit tube reader and Bioanalyzer and finally mixed at equal molarity to make the 20 nM pooled library for Illumina sequencing on a Illumina Novaseq X plus platform at BMKGENE GmbH.

Sequencing data analysis

UMIs (NNNNN) were extracted from the demultiplexed pair-end fastq files and appended to read identifiers by UMI-tools.[81] The adapters were trimmed by Cutadapt.[80] Read1 adapter to trim, AGATCGGAAGAGCACACGTCTGAACTCCAGTCAC; Read2 adapter to trim, GATCGTCGGACTGTAGAACTCTGAACGTGTAGATCTCGGTGGTCGCCGTATCATT. The processed reads were

pseudo-aligned and quantified at transcript level using Kallisto quant,[82] due to its outstanding ability to probabilistically assign multi-mapping reads to transcripts at high accuracy. The pseudo-alignment was done against the reference transcriptome of Gencode Release 47. The read counts for individual transcripts were normalized as RPMs. Plotting and statistical analysis, SRplot.[78]

Read count normalization on background RNA species

Rationales

As indicated by in-gel fluorescence (Figure 4H) and Bioanalyzer electropherograms (Figure S5A), SCOOPS_KO contains background RNA species intrinsically associated with the SCOOPS procedure, whereas SCOOPS_WT contains hepRNA as well as the background RNA. Thus, the background RNA could serve as an internal standard and provide a means to normalize sequencing data. This is similar to the idea of normalization on a minor set of genes/transcripts that remain unchanged between biological conditions, such as housekeeping genes and spike-in controls.[85] Unlike the routinely used median of ratios[86] or trimmed mean of M values[87] methods, which presumes only a small fraction of genes/transcripts differs between conditions, normalization on minor unchanging components is performed when a global shift is expected, which is the case for SCOOPS_WT and SCOOPS_KO.

If SCOOPS were performed with comparable cell numbers for WT and KO, the background RNA in SCOOPS interphase, which is intrinsic to the technique, should be of similar quantity in the two samples. Due to the presence of hepRNA, WT had substantially more RNA in the SCOOPS interphase (Stage 1, Figure S5D). However, equitizing masses of RNA input for sequencing library preparation led to the reduced background RNA present in SCOOPS_WT than in SCOOPS_KO (Stage 2). Such difference in background RNA species in WT and KO were kept throughout the entire process, particularly as both samples underwent the same number of PCR cycles (16 cycles), and were pooled in equimolar for sequencing (Stage 3). Upon normalization by library size (read count per million mapped reads, or RPM), the background RNA species in SCOOPS_WT should consistently have smaller RPMs than those in SCOOPS_KO (Stage 4). To make it a fair comparison between SCOOPS_WT and _KO, the background RNA in the former should be scaled to the same level as in the latter. The scaling factors for normalizing on background RNA should then be applied to all mapped genes/transcripts in each sample (Stage 5).

Scaling factors for normalization

Although external scaling factors could have been derived from comparing the amount of sequencing library input (150 ng) as fraction out of the total amount of SCOOPS isolated RNA in WT and KO samples, we deliberately avoided normalization by these external factors. Instead, we sought to derive the scaling factors internally, by comparing background RNA transcripts between SCOOPS_WT and KO datasets. We define background RNA as those with more than 2 times decrease in their mean RPMs in SCOOPS_WT compared to the _KO sample ($\log_2$FoldChange[WT/KO] < -1, with a $\log_2$RPM $\geq$ 5 filter. See rationales). Of this subset of transcripts, Pearson correlation analysis revealed high similarity (R = 0.97) between SCOOPS_WT and _KO (Figure S5E), which fits with the hypothesis that the background RNA is intrinsically associated with the SCOOPS procedure and remains unchanged between biological conditions. Library-specific scaling factors were then derived from performing median of ratios normalization for each SCOOPS sample (Figure S5F). Remarkably, such internal scaling factors correlate well with the external factors (Figure S5G). The RPMs for all transcripts in each individual library were then uniformly corrected by the corresponding internal scaling factor.

KIR2DL5 transfection, in-situ crosslinking and RNA co-precipitation

Wildtype (CHO-K1) and heparan sulfate-deficient cells (CHO pgsD-677) in a 10 cm dish at 70% confluency were transfected with 10 μg full-length KIR2DL5 plasmid (Addgene, #157623), using 2μl polyetherimide (PEI, 2mg/ml) per μg DNA in F-12K medium. 6h after transfection, the serum-free medium was replaced the one supplemented with 10% fetal bovine serum (FBS). The next day, cells were washed once with 1x DPBS following culture media removal. The cells were crosslinked in a Stratalinker for 5 min with the lid open. Once crosslinking is finished, the cells were scraped into 500μl per dish lysis buffer (50 mM Tris-HCl pH 7.4, 100 mM NaCl, 1% v/v NP-40, 0.1% v/v SDS and 0.5% w/v sodium deoxycholate) containing 1x cOmplete™ protease inhibitor cocktail (Roche, 11836153001). The cells were transferred into an Eppendorf tube and sonicated for 5 min (20% power, 5s on and 5s off). To the sonicated lysate was added 2 μl Turbo DNase, and 4 μl diluted RNase I (prediluted 1:20 in 1x DPBS). The lysate was then incubated at 37 °C for 5 minutes, followed by the addition of 2.5 μl SUPERaseIn. After centrifuging at 15,000g for 10 min at 4 °C, the supernatant was transferred to antibody-bound protein A beads (rabbit anti-DYKDDDDK tag antibody, Proteintech, 20543-1-AP; or rabbit IgG isotype control). The suspension was incubated on an end-to-end rotator at 4 °C for 2 h. The supernatant was magnetically separated and the beads were washed twice with 200 μl high-salt wash buffer (50 mM Tris-HCl pH 7.4, 1 M NaCl, 1% v/v NP-40, 1 mM EDTA, 0.1% v/v SDS and 0.5% w/v sodium deoxycholate), three times with 200 μl low-salt wash buffer (20 mM Tris-HCl pH 7.4, 10 mM $MgCl_2$, 0.2% v/v Tween-20 and 5 mM NaCl). The precipitated RNA-KIR2DL5 was 3'-end repaired and biotin ligated following the procedure described for TLR7-Fc. After the final wash, beads were directly taken up in 1x SDS sample loading buffer containing 1x sample reducing solution, denatured at 75°C for 10 minutes. The samples were resolved with SDS-PAGE, wet transferred onto a nitrocellulose (NC) membrane at 30 V for 4 hours at 4 °C, and subjected to chemiluminescent biotinylated nucleic acid detection using streptavidin-HRP (Thermo Fisher Scientific, 89880D). For Flag tag detection, the samples were resolved with SDS-PAGE, semi-dry transferred onto a polyvinylidene fluoride (PVDF) membrane at 25 V for 30 mins, and detected using rabbit anti-DYKDDDDK tag (Proteintech, 20543-1-AP, 1:10000) in combination with HRP-conjugated goat-anti-ribbit secondary antibody.

Biotinylation at total RNA fragments 3'-end (for *in vitro* KIR2DL5 binding)

Isolated total RNA was treated with Turbo DNase and then proteinase K to remove residual DNA and polypeptides. The purified RNA was fragmented with 4 μl 10x RNA Fragmentation Buffer (NEB, E6186AVIAL) added to 36 μl of total RNA in DEPC-treated water. The reaction was incubated at 94 °C for 2.5 minutes. Afterwards, 5 μl RNA Stop Solution (NEB, E6187AVIAL) was added. The fragmented RNA was kept on ice for over a minute was purified with the Zymo RCC-25 columns following the protocol provided by the supplier. To perfom end repair, 80 μg purified fragmented RNA was combined with 10 μl 10x PNK buffer, 5 μl FastAP (Thermo Fisher Scientific, EF0654), 1 μL SUPERase·In and 2 μl Turbo DNase, and incuabted at 37 °C for 30 minutes on a thermoshaker. The dephosphorylated RNA was combined with 1 ml TRIzol, from which the aqueous phase was mixed with an equivolume of ethanol and purified using Zymo RCC-25 columns. The RNA was eluted in 50 μl nuclease-free water. To the RNA solution, 14 μl 5x polymerase buffer (100 mM Tris-HCl pH 7.0, 3 mM $MnCl_2$, 0.1 mM EDTA, 1 mM DTT, 0.5 mg/ml acetylated BSA, 50% glycerol (v/v)), 5 μl yeast poly(A) polymerase (Jena Bioscience, RNT-006-S), 2'-Azido-2'-dATP (Jena Biosciences, NU-976S, 50 μM final concentration) and 0.5 μl SUPERase·In were added. The solution was incubated at 37 °C for 1 hour on a thermoshaker. The resulted RNA-3'-azide was purified as described for the end repair. Finally, 50 μl RNA-3'-azide was combined with 20 μl of 2x denaturing loading buffer (95% formamide, 25 mM EDTA). Next, the RNA was incubated with 1 mM of DBCO-PEG_4-biotin (Sigma, 760749) at 50 °C for 10 minutes. The biotinylated RNA was purified as described above.

In vitro KIR2DL5 binding, crosslinking, and RNA co-precipitation

The 3'-end biotinylated RNA described above was denatured in DEPC-treated water at 70 °C for 5 minutes and immediately put on ice. KIR2DL5-Fc (Biotechne, 6634-KR) or IgG isotype control (0.5 μg) were incubated with 2 μg biotinylated or non-biotinylated RNA in DPBS lysis buffer (1% NP-40 (v/v), 0.1% SDS (w/v), sodium deoxycholate 0.5% (w/v), 1x DPBS) at 16 °C with gentle shaking for 30 minutes. Afterwards, the samples were irradiated on ice with UVC (254nm) for 5 minutes. Next, the samples were resolved on a 12% SDS-PAGE gel, wet transferred onto a nitrocellulose (NC) membrane at 30 V for 4 hours at 4 °C and subjected to chemiluminescent detection of biotinylated nucleic acid. The same NC membrane was subjected to Western blot for human Fc detection using AlexaFulor488-conjugated goat-anti-human IgG.

AlphaFold3 prediction of structural model for KIR2DL5 and potential interacting partners

The predicted results can be found in Figure S6. The prediction was performed using AlphaFold Server (https://alphafoldserver.com/). The sequence of KIR2DL5 extracellular domain (aa 22 – 238) was used as input. To predict nucleic acid interactions, octanucleotide repeats (A_8, U_8, G_8 and C_8) were used as input.

To investigate if KIR2DL5 binding to the cell surface may be mediated by any of the cell-surface RBP hits, the sequences of hits from the TLR7-proximal were obtained from Uniprot and used directly as another protein entity. Among all tested cell-surface RBPs, none gave an acceptable ipTM score (all below 0.6). Furthermore, we also observed a decrease of local plDDT scores for KIR2DL5 at the predicted interface compared to KIR2DL5 alone. Such worsened plDDT scores and low ipTM values indicate KIR2DL5 is unlikely to interact, at least, any of the screened cell-surface RBPs.

We further employed AF3 to gain insights into the molecular function of KIR2DL5-RNA association. KIR2DL5 belongs to the immunoglobulin superfamily (IGSF), and numerous members within this superfamily undergo homophilic interactions. We asked if homophilic interactions between KIR2DL5 monomers may occur and if RNA might regulate the oligomer/monomer states of KIR2DL5. We set the copy numbers of KIR2DL5 to 2, with or without a stretch of guanosine repeats with varying lengths (G_8, G_{12}, G_{16} and G_{20}) as another entity.

QUANTIFICATION AND STATISTICAL ANALYSIS

Statistical analysis was performed using GraphPad Prism (10.4.1), Matplotlib (3.7), or SRplot.[78] Sample sizes (n) are stated in the corresponding figure captions. Figures 1C, 2E, S2G, and S6C employed the unpaired ordinary one-way ANOVA and Dunnett's multiple comparisons. In Figure 2B, sigmaFC values are given to each gene based on all fold changes of gRNAs targeting a gene and the number of significant gRNAs for the gene, which is a built-in function of PinAPL-Py.[79] The sigmaFC values displayed on the graph are geometric means of those from two independent replicates. In the volcano plots (Figures 3C and 3D), the $\log_2$(Fold Change) values are based on the LFQ values calculated using the built-in workflow of Proteome Discoverer version 3.1 (see method details). The P values were derived from three independent replicates using unpaired, two-tailed Student t-test. Figures 4G and 4H employed unpaired, two-tailed Welch's t-test. Figures 6C and 6D used the unpaired, two-tailed multiple t-test (equal variance) with Holm-Šidák correction. Figures S6A, S6B, and S6D used unpaired, two-tailed Student's t-test. In Figure 5B, paired data (transcript RPM values in wildtype and HS-deficient cells) were analyzed using the Wilcoxon signed-rank test (two-tailed). In Figures 5F and 5G, the high- and low-confidence hepSNORD were compared using unpaired, two-tailed Mann-Whitney U test.